





ALMA Observations of Molecular Clouds in Three Group-centered Elliptical Galaxies: NGC 5846, NGC 4636, and NGC 5044

Pasquale Temi¹ , Alexandre Amblard^{1,2}, Myriam Gitti^{3,4}, Fabrizio Brighenti³, Massimo Gaspari^{5,8} ,
William G. Mathews⁶, and Laurence David⁷

¹ Astrophysics Branch, NASA Ames Research Center, Moffett Field, CA, USA

² BAER Institute, Sonoma, CA, USA; pasquale.temi@nasa.gov

³ Physics and Astronomy Department, University of Bologna, Via Gobetti 93/2, I-40129, Bologna, Italy

⁴ INAF, Istituto di Radioastronomia di Bologna, Via Gobetti 101, I-40129 Bologna, Italy

⁵ Department of Astrophysical Sciences, Princeton University, Princeton, NJ 08544, USA

⁶ University of California Observatories/Lick Observatory, Department of Astronomy and Astrophysics, University of California, Santa Cruz, CA 95064, USA

⁷ Harvard-Smithsonian Center for Astrophysics, 60 Garden St., Cambridge, MA 02138, USA

Received 2017 November 26; revised 2018 March 18; accepted 2018 March 20; published 2018 April 27

Abstract

We present new ALMA CO(2–1) observations of two well-studied group-centered elliptical galaxies: NGC 4636 and NGC 5846. In addition, we include a revised analysis of Cycle 0 ALMA observations of the central galaxy in the NGC 5044 group. We find evidence that molecular gas is a common presence in bright group-centered galaxies (BGG). CO line widths are broader than Galactic molecular clouds, and using the reference Milky Way X_{CO} , the total molecular mass ranges from $2.6 \times 10^5 M_{\odot}$ in NGC 4636 to $6.1 \times 10^7 M_{\odot}$ in NGC 5044. Complementary observations using the ALMA Compact Array do not exhibit any detection of a CO diffuse component at the sensitivity level achieved by current exposures. The origin of the detected molecular features is still uncertain, but these ALMA observations suggest that they are the end product of the hot gas cooling process and not the result of merger events. Some of the molecular clouds are associated with dust features as revealed by *HST* dust extinction maps, suggesting that these clouds formed from dust-enhanced cooling. The global nonlinear condensation may be triggered via the chaotic turbulent field or buoyant uplift. The large virial parameter of the molecular structures and correlation with the warm (10^3 – 10^5 K)/hot ($\geq 10^6$) phase velocity dispersion provide evidence that they are unbound giant molecular associations drifting in the turbulent field, consistent with numerical predictions of the chaotic cold accretion process. Alternatively, the observed large CO line widths may be generated by molecular gas flowing out from cloud surfaces due to heating by the local hot gas atmosphere.

Key words: galaxies: active – galaxies: elliptical and lenticular, cD – galaxies: groups: general – galaxies: ISM

1. Introduction

Local brightest-group galaxies (BGGs) are prime systems to study the physics of the hot interstellar or intergroup medium, including its connection with the central massive black hole and the associated active galactic nucleus (AGN) feedback. They are in many respects simple objects, where hot gas cooling and evolution can be investigated without other complicating processes, like star formation or gas-rich merging (e.g., Feldmann et al. 2010; O’Sullivan et al. 2017).

In fact, the most massive group-centered elliptical galaxies have red and old stellar populations, with little or no evidence of recent star formation (Daddi et al. 2005; van der Wel et al. 2005; Ziegler et al. 2005; Werner et al. 2014; Gozaliasl et al. 2016). The three galaxies we have selected for this study, NGC 4636, NGC 5044, and NGC 5846, are perfect examples of passive systems, with very old stellar populations (Trager et al. 2000; Annibali et al. 2006; Diniz et al. 2017) and star formation rates on the order of a few percent $M_{\odot} \text{ yr}^{-1}$ (Werner et al. 2014).

Central galaxies in massive clusters have higher X-ray luminosities and are much richer in warm/cold interstellar medium (ISM), with molecular gas masses $M_{\text{H}_2} \sim 10^9$ – $10^{11} M_{\odot}$ (Edge 2001; Salomé and Combes 2003; Pulido et al. 2017). However, they are located at distances ≥ 100 Mpc and usually inhabit complex environments—e.g., affected by merging, stripping, star formation, and supernovae—which makes it difficult to fully unveil the gas cooling process and its connection to the feedback mechanism.

The absence or dearth of star formation in BGGs is remarkable. These galaxies usually have a massive hot gas halo radiating away 10^{41} – $10^{43} \text{ erg s}^{-1}$ (Mathews & Brighenti 2003; Sun 2012; Anderson et al. 2015; Goulding et al. 2016). This corresponds to a cooling rate $\dot{M}_{\text{cool}} \sim 1$ – $50 M_{\odot} \text{ s}^{-1}$ if radiative losses are not balanced by some form of heating. Evidently, a continuous gas heating or removal mechanism is required to halt star formation. Since all of these galaxies harbor supermassive black holes (SMBHs), it is natural to expect that the AGN feedback process plays a pivotal role in regulating the gas cooling (e.g., Croton et al. 2006; McNamara & Nulsen 2007; Gitti et al. 2012).

Indeed, *Chandra* and *XMM* observations have shown that hot gas ($T \sim 10^7$ K) cooling is suppressed by more than an order of magnitude with respect to the classical cooling flow expectation (e.g., McNamara & Nulsen 2007; Peterson et al. 2003; Peterson & Fabian 2006; McNamara & Nulsen 2012; Molendi et al. 2016). This is true at all mass scales, from

⁸ Einstein and Spitzer Fellow.

galaxies to clusters. X-ray images clearly show that the SMBH strongly interacts with its environment, generating outflows/jets, bubbles, turbulence, and shocks that heat the surrounding hot atmosphere (e.g., McNamara & Nulsen 2007; Fabian 2012 for a review).

Multiwavelength observations of massive ellipticals nevertheless show a multiphase ISM, suggesting that residual cooling occurs and regulates the triggering of the AGN and galaxy evolution. $H\alpha$ emission is regularly detected (e.g., Caon et al. 2000; McDonald et al. 2011; Sarzi et al. 2013; Werner et al. 2014) and probes photoionized warm $T \sim 10^4$ K gas (Haardt & Madau 2012). The warm gas typically occupies an irregular region several kpc in size and displays a complex and chaotic kinematics. Dust associated with both the hot and cold ISM phases is also often detected (Temi et al. 2009; Smith et al. 2012; O’Sullivan et al. 2015). Recent observations have shown that [C II] emission is also a common presence in massive ellipticals (Werner et al. 2014). The [C II]- and $H\alpha$ -emitting gas is largely cospatial, which suggests that [C II] emission also traces the warm phase. While a significant fraction of the cold gas mass in low- to intermediate-mass early-type galaxies (ETGs) is thought to have an external, merger-related origin (e.g., Davis et al. 2011), in the most massive ETGs, of interest here, the cold and warm gas phases are likely generated by in situ cooling (Davis et al. 2011; David et al. 2014; Werner et al. 2014).

Recent theoretical developments have shown that, while AGN-generated outflows and cavities globally inhibit cooling, they also stimulate residual cooling in spatially extended regions ~ 1 –10 kpc in size, where the ratio of the cooling time to freefall time is $t_{\text{cool}}/t_{\text{ff}} \lesssim 10$ –30 (Revaz et al. 2008; Gaspari et al. 2011, 2017b; Sharma et al. 2012; Brighenti et al. 2015; Li et al. 2015; Valentini & Brighenti 2015; Voit et al. 2015; Barai et al. 2016; Lau et al. 2017).

The multiphase condensation mechanism might be related to the feeding of SMBHs through the so-called chaotic cold accretion (CCA) mechanism (e.g., Gaspari et al. 2013, 2015, 2017b). In this scenario, warm filaments and cold clouds condense out of the hot halo and recurrently boost the accretion rate up to a few orders of magnitude compared with hot (Bondi) accretion. The AGN responds by injecting back the energy in the form of entrained massive outflows and/or relativistic jets, establishing a tight self-regulated loop (e.g., see Gaspari and Sądowski 2017 for a brief review). During CCA, the gas phases are spatially and kinematically correlated, showing comparable cooling and eddy turnover time $t_{\text{cool}}/t_{\text{eddy}} \approx 1$ (Gaspari et al. 2017a).

Currently, the coldest ISM phase (molecular or neutral gas) in normal massive elliptical galaxies is the least studied and not well characterized. Recent ALMA observations of the galaxy group NGC 5044 have revealed approximately 20 CO-emitting clouds in the central 10 kpc of the galaxy (David et al. 2014). In this paper, we present new ALMA CO(2–1) observations of two group-centered elliptical galaxies (NGC 4636 and NGC 5846) to seek confirmation that molecular gas is a common presence in BGGs and that it is not a result of merger events but rather has cooled directly from the hot gas. In addition, we include a revised analysis of the Cycle 0 ALMA observations of NGC 5044 that were previously published by David et al. (2014). The current, more reliable pipeline is used to reduce ALMA Cycle 0 data, known to suffer from early calibration issues. These three galaxies have the most complete

observational coverage, with available deep *Chandra* X-ray data, SOAR and *HST* $H\alpha$ observations, *Herschel* [C II] data, *Spitzer* FIR data, and detailed *HST* dust absorption maps. All three galaxies satisfy the empirical criteria for extended multiphase gas cooling (Gaspari et al. 2013; Brighenti et al. 2015; Valentini & Brighenti 2015; Voit et al. 2015, 2017; Pulido et al. 2017 and references therein): central entropy $\lesssim 15$ keV cm² at radii of 5–15 kpc, minimum $t_{\text{cool}}/t_{\text{ff}} \lesssim 20$, $t_{\text{cool}} \lesssim 3 \times 10^8$ yr, and $t_{\text{cool}}/t_{\text{eddy}} \approx 1$. Equally important, they all exhibit X-ray evidence of recent feedback, bubbles, and radio emission, and each is expected to have low-entropy regions that are currently cooling (Gaspari et al. 2013; Brighenti et al. 2015; Valentini & Brighenti 2015; Voit et al. 2015, 2017).

2. Galaxies Sampled

In this section, we describe in depth the two galaxies for which new CO(2–1) data have been collected. We refer to David et al. (2014) for a description of NGC 5044. With the adopted distances of 31.2, 24.2, and 17.1 Mpc for NGC 5044, NGC 5846, and NGC 4636 (Tonry et al. 2001), the corresponding physical scales are 151, 118, and 83 pc arcsec^{−1}, respectively. Table 1 shows a summary of the two galaxies properties.

2.1. NGC 5846

NGC 5846, spherical in shape, is classified as a giant elliptical E0 and is the central and brightest galaxy in its group (Mahdavi et al. 2005).

Its proximity makes this object one of the closest examples of AGN feedback in massive ellipticals. This is a very well-studied system in every wavelength other than at radio frequencies (Machacek et al. 2011). There is good knowledge of its hot ($\sim 10^7$ K) and ionized medium, while little is known about the content and dynamics of the cold ($\leq 10^4$ K) phase, likely a significant component in the central kpc or so.

The dramatic effects of AGN outflows in NGC 5846 were first discovered in the X-ray band, which probes hot ($\approx 10^7$ K) gas (Trinchieri & Goudfrooij 2002; Machacek et al. 2011). Two inner bubbles in the hot gas, at a distance of 600 pc from the center and filled with radio emission, are clear indications of recent AGN feedback. A weak radio source, elongated in the NE–SW direction, connects the inner cavities. X-ray-bright rims surround the inner X-ray bubbles (Machacek et al. 2011). Many X-ray knots are visible, suggesting cooling sites. The scenario indicated by the *Chandra* observation is that of an AGN outflow, compressing and cooling the gas (e.g., Brighenti et al. 2015) in the central ~ 2 kpc ($20''$ at the distance of NGC 5846).

$H\alpha$ observations (Caon et al. 2000; Trinchieri & Goudfrooij 2002; Werner et al. 2014) reveal the presence of warm ($T \sim 10^4$ K) ionized gas in the inner 2 kpc of NGC 5846. Spectra of this gas indicate irregular motion, with a typical velocity of 150–200 km s^{−1}. The warm 10^4 K gas traces the X-ray-bright features, again suggesting a multiphase AGN outflow.

Using the *Spitzer* IRS, Rampazzo et al. (2013) detected mid-infrared lines (e.g., [Ne II] 12.81 μm , [Ne III] 15.55 μm) but no trace of polycyclic aromatic hydrocarbon (PAH) emission. Filho et al. (2004) identified several sources in the radio at 2.3, 5, and

15 GHz using VLBA data; these sources are aligned in the south–north direction.

Recent *Herschel* PACS observations have detected the presence of [C II]-emitting gas that extends to a radius of ~ 2 kpc and is centrally peaked. The [C II] emission is almost exactly cospatial with the $H\alpha$ + [N II] emission, and the total fluxes in [C II] and $H\alpha$ + [N II] have a ratio $F_{H\alpha+[NII]}/F_{[CII]} = 2.5$, a very similar flux ratio value observed in other group-centered ellipticals (Werner et al. 2014). Furthermore, the velocities inferred from the [C II] line are consistent with those measured for the $H\alpha$ line (Caon et al. 2000). All of this evidence suggests that the [C II] line is emitted by the warm gas, and it is not necessarily tracing the molecular phase.

NGC 5846 has another indication that the cold gas is being disturbed by an AGN outburst. It has, in fact, an excess of cold ($T \sim 30$ K) dust approximately cospatial with the ionized and molecular gas (Temi et al. 2007b; Mathews et al. 2013). With a $70 \mu\text{m}$ luminosity of $3.5 \times 10^{41} \text{ erg s}^{-1}$ (Temi et al. 2009), NGC 5846 shares the same dust properties as several giant ellipticals (e.g., NGC 4636 and NGC 5044; Temi et al. 2007a), which are best explained with the ejection of dusty gas from their centers by AGN activity that occurred $\sim 10^7$ yr ago. This dust has to still be embedded in the cold gas, otherwise it would be sputtered away in $\sim 10^7$ yr.

2.2. NGC 4636

NGC 4636 is the central galaxy of a poor group in the outskirts of the Virgo Cluster. It harbors a relatively small SMBH of $7.9 \times 10^7 M_{\odot}$ (Merritt & Ferrarese 2001), as inferred from the bulge velocity dispersion.

The dramatic effects of AGN outflows in NGC 4636 were first discovered in the X-ray band, which probes the hot ($\approx 10^7$ K) gas (Jones et al. 2002; Baldi et al. 2009). Large bubbles in the hot gas, surrounded by bright rims, are likely the result of shocks generated by the AGN jets. A weak radio source, elongated in the NE–SW direction, connects the NE and SW bubbles.

Of major interest is the X-ray-bright core, having a radius of ~ 1 kpc. As discussed in Baldi et al. (2009), the core shows a central cavity surrounded by a bright edge. Interestingly, the small X-ray cavity surrounds the ~ 1 kpc radio jet detected at 1.4 GHz (Allen et al. 2006) and is likely generated by the jet. Thus, the X-ray and radio observations point to a scenario in which gas may be currently outflowing in the central kpc of NGC 4636. UV emission (Bregman et al. 2001, 2005) exhibits O VI emission, which is a tracer of gas cooling. The measured emission indicates a cooling rate of $0.3 M_{\odot} \text{ yr}^{-1}$. Rampazzo et al. (2013) detected PAH emission at 11.3 and $17 \mu\text{m}$, as well as [Ne II], [Ne III], and [S III] lines in the center of NGC 4636 (within $r_e/8$) using the *Spitzer* IRS. $H\alpha$ observations (Caon et al. 2000; Werner et al. 2014) reveal the presence of warm ($T \sim 10^4$ K) ionized gas in the inner kpc of NGC 4636. Spectra of this gas indicate irregular motion, with a typical velocity of $150\text{--}200 \text{ km s}^{-1}$. $H\alpha$ maps of the galaxy core show the presence of a cavity in the distribution of the ionized gas encircled by a dense shell located at a distance of ~ 400 pc from the center. Again, the most plausible explanation is gas expansion caused by AGN activity.

In NGC 4636, the [C II] emission extends to a radius of ~ 1 kpc and is centrally peaked. The velocities inferred from the [C II] line are consistent with those measured for the $H\alpha$ line. Finally, NGC 4636 has an excess of cold dust, approximately cospatial

Table 1
Summary of NGC 5846 and NGC 4636 Properties

	NGC 5846	NGC 4636
AGN	Yes	Yes
AGN kinetic power (erg s^{-1})	7.5×10^{41}	3×10^{41}
$L_{H\alpha+[NII]}$ (erg s^{-1})	2.5×10^{40}	6×10^{39}
PAH lines (μm)	...	11.3, 17
Distance (Mpc)	24.2	17.1
ATLAS ^{3D} classification	Slow rotator	Slow rotator
Effective radius (arcsec, kpc)	59, 6.9	89, 7.4
Radio power (erg s^{-1})	2.5×10^{38}	1.5×10^{38}

Note. As Measured or Referenced in Caon et al. (2000), Tonry et al. (2001), Trinchieri & Goudfrooij (2002), Allen et al. (2006), Mei et al. (2007), Cavagnolo et al. (2010), Cappellari et al. (2011), Emsellem et al. (2011), Rampazzo et al. (2013), and Werner et al. (2014)

with the ionized and molecular gas (Temi et al. 2007a; Mathews et al. 2013). As above, this dust is expected to be embedded in cold gas, to be protected against rapid sputtering. In Temi et al. (2007a), we showed that the extended dust distribution originates from the ejection of cold gas by AGN activity 10 Myr ago.

3. Observations and Data Reduction

3.1. New Cycle 3–4 Observations of NGC 5846 and NGC 4636

We observed NGC 5846 and NGC 4636 with ALMA during Cycle 3 (project code: 2015.1.00860.S; PI: Temi). For both galaxies, the ALMA interferometer was configured such that its longest baseline was about 640 m and its shortest baseline about 15 m. This configuration resulted in an angular resolution of about $0''.6$ and a maximum recoverable scale of $5''.4$. Assuming a distance of 17.1 Mpc for NGC 4636 and 24.2 Mpc for NGC 5846, $0''.6$ and $5''.4$ correspond to 50 and 450 pc for NGC 4636 and 72 and 644 pc for NGC 5846, respectively. All data were taken in ALMA Band 6, one spectral window (spw) was centered around the CO (2–1) line, and three other spws measured the continuum. A detailed description of the observations is presented in Table 2.

The data were reduced using the CASA software (version 4.5.3; McMullin et al. 2007). As a first step, we carefully checked the results of the quality assurance (QA) processes provided by the Science Pipeline team, focusing in particular on the calibration process. For NGC 5846, the pipeline calibration appears to be reasonable; therefore, we simply produced the calibrated data set by running the original pipeline reduction scripts. We further attempted the self-calibration, but the image quality did not improve. For NGC 4636, a bad antenna (DV02) partially corrupted the second execution block (EB); therefore, we flagged it and performed a new manual calibration following the steps in the script provided to the PI and then combined the two EBs to produce the final calibrated data set. Self-calibration was attempted as well, but no good solutions were found.

The continuum-subtracted cubes were produced using the CLEAN algorithm provided in the CASA package, and several velocity resolutions, Briggs weightings, and threshold values were explored to determine the optimum setup for each image and investigate the goodness of the detection. In the end, we used in this paper two thresholds to produce maps that will be used to detect the potential signals. One threshold corresponds to about 1.5 times the noise rms of the treated data; it is a more

Table 2
Summary of ALMA Observations of NGC 5846 and NGC 4636

Observation center (R.A., Decl.)	NGC 5846		NGC 4636	
	(15 ^h 6 ^m 29 ^s .253, 1°36'20"290)		(12 ^h 42 ^m 49 ^s .867, 2°41'16"010)	
Observation dates (yyyy mm dd)	ALMA 12 m			
	2016 May 13		2016 May 02	2016 May 03
Observation duration (minutes)	71.15		49.21	48.81
On-target duration (minutes)	40.82		29.74	29.74
PWV (mm)	1.08		1.12	2.02
T_{sys} at 230 GHz (K)	75		74	90
Calibrators (flux, bandpass, phase)	J1517–2422, J1550 +0527, J1505+0326		J1229+0203	
Line central wavelength (GHz)	229.23		229.83	
Line bandwidth and resolution (MHz, km s ⁻¹)			(937.5, 1200) and (0.5, 0.6)	
Continuum central wavelengths (GHz)	216.45, 218.17, 230.61		215.62, 217.33, 229.91	
Continuum bandwidth and resolution (MHz, km s ⁻¹)			(1850, 2400) and (31.25, 42)	
Observation dates (yyyy mm dd)	ALMA Compact Array (ACA)			
	2016 Dec 21	2017 Apr 29	2016 Dec 28	2017 Mar 26
Observation duration (minutes)	77.13	77.31	91.62	91.55
On-target duration (minutes)		34.27		49.90
T_{sys} at 230 GHz (K)	86	68	61	64
Calibrators (flux, bandpass, phase)	Callisto, J1256–0547, J1516 +0015		J1256–0547, J1229+ 0203, J1229+0203	
Line central wavelength (GHz)	229.23		229.83	
Line bandwidth and resolution (MHz, km s ⁻¹)			(937.5, 1200) and (0.5, 0.6)	
Continuum central wavelengths (GHz)	214.02, 215.71, 228.02		214.33, 216.02, 228.52	
Continuum bandwidth and resolution (MHz, km s ⁻¹)			(1850, 2400) and (31.25, 42)	

aggressive “cleaning” version. A lower threshold creates a lot of sources that most likely are just noise. The other threshold corresponds to about 4 times the noise rms of our data; it is a more conservative “cleaning.” Using a much larger threshold would correspond to making a final image that is identical to the initial dirty map, since the signal-to-noise ratio (S/N) in our data is not very large and the algorithm would not find any signal to iterate on. Using thresholds between these two values does not produce significantly different results with our data. Table 3 indicates with which threshold a source has been detected. The CO maps in the figures have been produced using the more aggressive threshold, since it returns a better S/N on maps.

In this paper, we present images and spectra obtained with 10 km s⁻¹ resolution image cubes and natural weighting (robustness parameter = 2) with the CLEAN algorithm running in noninteractive mode (threshold = 0.5 mJy, which roughly corresponds about 1.5 times the rms noise). This provided a synthesized beam of 0".79 × 0".70 with a position angle (P.A.) of 79° for NGC 5846 observations and a synthesized beam of 0".74 × 0".67 with a P.A. of 116° for NGC 4636. For the reasons explained above, the final images presented here are not self-calibrated. The rms noise in the line-free channels was 0.02 and 0.01 mJy beam⁻¹ (primary beam corrected) for NGC 5846 and NGC 4636, respectively. Images of the continuum emission were also produced by averaging channels free of any line emission. An unresolved central continuum source is detected in both NGC 5846 and NGC 4636 with a flux of 10.63 ± 0.03 mJy at 220.997 GHz and 0.4 ± 0.1 mJy at 221.390 GHz, respectively. The position of the continuum is in good agreement with radio and optical images with an offset of 0".10 ± 0".01 and 0".15 ± 0".01 for NGC 4636 and NGC 5846, respectively.

In addition to the ALMA 12 m array observations, we obtained complementary data from the ALMA Compact Array (ACA) for NGC 5846 and NGC 4636 in Cycle 4 (project code: 2016.1.00843.S; PI: Temi). As for the 12 m observations, all data were taken in ALMA Band 6 with a similar spectral setup. These observations are presented in more detail in Table 2.

We used the products provided by the ALMA pipeline for the ACA data. The pipeline used CASA 4.7.2 and 4.7.38335 for NGC 5846 and NGC 4636, respectively. Using the Briggs-weighting scheme with a robust parameter of 0.5, the resulting beam size was 7".0 × 4".5 and 6".8 × 4".4 for NGC 5846 and NGC 4636, respectively. The final estimates of the rms noise values are 4.02 and 2.45 mJy beam⁻¹ for NGC 5846 and NGC 4636 with a velocity bin of 10 km s⁻¹.

3.2. Reanalysis of Cycle 0 Observations of NGC 5044

NGC 5044 was observed during Cycle 0 (project code: 2011.0.00735.SSB; PI: Lim) and is described in detail in David et al. (2014); here we only summarize the main characteristics of these observations. NGC 5044 was observed with an angular resolution of 2".0 × 1".4 for 29 minutes with a spectral resolution of 0.64 km s⁻¹ around the CO(2–1) emission line.

Given the uncertainties associated with the early phase of ALMA data reduction and calibration, we decided to again reduce the NGC 5044 observations with the latest release of the CASA reduction and calibration software package. In particular, we followed the CASA guides⁹ to modify the packaged calibration script in order to apply the proper amplitude calibration scale (which has changed since Cycle 0) and remove some atmospheric lines in the calibrators. The channels containing these lines were

⁹ https://casaguides.nrao.edu/index.php/Guide_To_Reddo_Calibration_For_ALMA_Cycle_0; https://casaguides.nrao.edu/index.php/Updating_a_script_to_work_with_CASA_4.2

Table 3
Cloud Candidates for NGC 5846, NGC 4636, and NGC 5044

ID	(R.A., decl.) offset (arcsec), (kpc)	$\langle v \rangle$ (km s ⁻¹)	σ (km s ⁻¹)	$S_{\text{CO}}\Delta v$ (Jy km s ⁻¹)	S/N	M_{mol} (10 ³ M _⊙)	Ang. Size FWHM (arcsec)	Phys. Size (pc)	Methods
NGC 5846									
1	(-2.3,-1.5), (-0.3,-0.2)	-230.7 ± 1.6	23.3 ± 1.6	0.32 ± 0.02	19.6	6.4 ± 0.4	1.2±0.2 ×0.2±0.2	143 × 24	I,F,i,f
2	(-0.8,-18.0), (-0.1,-2.1)	-155.4 ± 3.0	14.6 ± 3.0	0.24 ± 0.04	8.0	4.8 ± 0.8	<0.7	<82	i,f
3	(8.2,3.2), (1.0,0.4)	110.6 ± 1.6	19.9 ± 1.6	0.45 ± 0.04	14.2	8.9 ± 0.7	2.9±0.3 ×0.7±0.04 [†]	346 × 83	I,F,i,f
NGC 4636									
1	(-19.0,-0.3), (-1.6,-0.0)	140.3 ± 8.4	26.4 ± 8.4	0.20 ± 0.06	6.7	1.9 ± 0.5	<0.7	<50	i,f
2	(2.0,0.3), (0.2,0.0)	209.5 ± 3.9	25.8 ± 3.9	0.07 ± 0.01	12.4	0.7 ± 0.1	<0.7	<50	I,F,i,f
NGC 5044									
1	(-0.1,-2.0), (-0.0,-0.3)	-556.9 ± 11.9	67.0 ± 10.7	0.8 ± 0.1	11.7	24.4 ± 3.8	<2.0	<300	I,F,i,f
2	(0.0,2.8), (0.0,0.4)	-313.1 ± 9.5	36.6 ± 9.4	0.4 ± 0.1	6.2	12.2 ± 2.5	<2.0	<300	I,F,i,f
3	(-2.2,-1.4), (-0.3,-0.2)	-274.4 ± 4.5	28.4 ± 4.4	0.4 ± 0.1	10.6	12.8 ± 1.8	<2.0	<300	F,i,f
5	(-12.0,-5.2), (-1.8,-0.8)	-192.8 ± 6.6	30.5 ± 8.5	0.7 ± 0.1	7.7	23.2 ± 3.8	<2.0	<300	F,i,f
6	(-1.9,1.8), (-0.3,0.3)	-226.8 ± 4.3	20.4 ± 4.3	0.3 ± 0.1	8.2	9.5 ± 1.8	<2.0	<300	I,F,i,f
7	(-1.3,6.4), (-0.2,1.0)	-207.0 ± 6.9	31.1 ± 6.4	0.4 ± 0.1	7.3	12.6 ± 2.5	<2.0	<300	F,i,f
8	(-0.4,-0.4), (-0.1,-0.1)	-148.8 ± 8.2	76.2 ± 7.2	1.1 ± 0.1	14.3	33.9 ± 3.1	3.9±1.3 ×1.2±0.6	590 × 182	I,F,i,f
11	(3.0,-2.6), (0.5,-0.4)	-95.8 ± 6.0	41.0 ± 4.9	0.5 ± 0.1	10.1	16.5 ± 2.4	<2.0	<300	F,i,f
12	(-8.6,3.4), (-1.3,0.5)	-132.9 ± 3.9	18.4 ± 3.9	0.4 ± 0.1	6.6	13.6 ± 2.5	<2.0	<300	F,i,f
13	(-1.2,-2.4), (-0.2,-0.4)	-80.9 ± 6.9	43.1 ± 8.1	0.8 ± 0.1	12.0	26.0 ± 2.6	3.8±1.0 ×0.7±0.7	575 × 106	I,F,i,f
14	(-14.4,-5.8), (-2.2,-0.9)	-46.8 ± 10.6	39.0 ± 8.2	1.0 ± 0.2	9.1	30.7 ± 7.2	3.1±1.3 ×1.0±0.6	469 × 151	F,i,f
18	(0.8,1.2), (0.1,0.2)	27.8 ± 1.7	37.4 ± 1.7	3.0 ± 0.1	34.1	93.8 ± 3.7	1.9±0.2 ×0.8±0.5	287 × 121	I,F,i,f
20	(-15.0,-7.8), (-2.3,-1.2)	29.2 ± 12.8	73.0 ± 12.8	1.2 ± 0.2	8.9	37.6 ± 6.0	<2.0	<300	F,i,f
21	(-8.4,11.0), (-1.3,1.7)	41.8 ± 9.3	46.8 ± 8.4	1.0 ± 0.2	8.8	32.0 ± 5.5	<2.0	<300	F,i,f
22	(1.2,14.4), (0.2,2.2)	-18.3 ± 26.1	125.6 ± 24.6	1.7 ± 0.3	6.6	53.2 ± 9.0	<2.0	<300	F,i,f
25	(17.3,10.4), (2.6,1.6)	-573.7 ± 3.2	10.3 ± 2.1	0.7 ± 0.2	6.4	22.8 ± 6.6	<2.0	<300	i,f
26	(15.8,-12.8), (2.4,-1.9)	-108.1 ± 3.3	10.9 ± 3.4	0.6 ± 0.2	10.5	19.2 ± 5.4	<2.0	<300	i,f

Note. Cloud candidates for NGCQ3 5846 (top), NGC 4636 (center), and NGC 5044 (bottom) with their location with respect to the Galaxy center (offset along R.A., decl. axis in arcsec and kpc), their average velocity, their velocity dispersion, their total CO(2–1) flux (corrected from the primary beam effect), the S/N, the corresponding molecular mass calculated using Equation (1), the dimensions of the cloud (in arcsec and pc), and the methods with which the clump was detected (i when detected in the image, f when detected in the spectrum with a 1.5 noise rms cleaning threshold, and I and F when detected with a 4 noise rms cleaning threshold). To be consistent with cloud labeling in David et al. (2014), the original cloud number sequence for NGC 5044 has been maintained. The spectral properties have been calculated with a Gaussian fitted on the sum of the emission from pixels with an S/N larger than 4. The dimensions of the cloud were calculated with the *imfit* function of CASA and correspond to the deconvolved FWHM: for cloud 3 of NGC 5846, the dimensions of the cloud are not deconvolved from the beam, given that the minor-axis length is too close to the beam size.

further removed from the calibrated target in order to perform a correct continuum subtraction.

Similarly to what was done for NGC 5846 and NGC 4636, here we present the images and spectra obtained with 10 km s⁻¹ resolution image cubes and natural weighting with the CLEAN algorithm running in noninteractive mode (threshold = 1.6 mJy, which roughly corresponds to 1.5 times the rms noise). This provided a synthesized beam of 1.''99 × 1.''41 with a P.A. of 148°. The rms noise in the line-free channels was 1.0 mJy beam⁻¹.

4. Results

Using Cycle 0 ALMA observations, David et al. (2014) discovered over 20 CO(2–1)-emitting clouds in the brightest X-ray galaxy/group NGC 5044. With our new ALMA Cycle 3 observations, we seek confirmation that CO molecular clouds are common features in group-centered elliptical galaxies that are, in many respects, similar to NGC 5044.

In order to identify CO clouds in our data, we used the cubes described previously and three other sets of cubes for each galaxy. One set was produced by increasing the threshold of the cleaning algorithm to 1.5 mJy for NGC 5846 and NGC 4636 and 4 mJy for NGC 5044 (roughly 4 times the

rms noise) from 0.5 and 1.6 mJy. Two extra sets were produced by refining the velocity resolution to 3 km s⁻¹ and setting the CLEAN threshold to 0.9 and 2.5 mJy for NGC 5846 and NGC 4636 and to 1.6 and 7 mJy for NGC 5044, respectively (thresholds were scaled with the bin size, $\sqrt{10/3}$). This thinner spectral resolution is needed to perform the detection of the lines in the spectral domain. Our detection technique requires convolving the signal by a Gaussian kernel as thin as 9 km s⁻¹ wide, and the 3 km s⁻¹ provides an adequate sampling to do so.

With each 10 km s⁻¹ cube (two per galaxy), we identified clouds in each image by detecting pixels with a flux larger than 5 times the rms noise. These sets of pixel channels are then clustered together (spatially and between velocity channels) to form a list of cloud candidates.

With each 3 km s⁻¹ cube (two per galaxy), we whitened the noise by multiplying each pixel frequency stream by a function in Fourier mode that well approximates the noise power spectrum of these time streams; this operation reduces the effect of the Hanning filter introduced by the ALMA processing. We then convolved each pixel spectra by Gaussian kernels of various widths ($\sigma = 9, 18, 30, 45,$ and 60 km s⁻¹) and selected pixels with signals larger than 5 times the rms noise. Again, we clustered these lists of pixel velocity to obtain a list of cloud candidates.

Both of these techniques are tuned to measure lines larger than about 10 km s^{-1} , given that one is using a 10 km s^{-1} bin size and the other has a smallest kernel of 9 km s^{-1} . Using a thinner spectral resolution is very challenging with the data collected that do not have a large S/N. Furthermore, given the angular resolution of these observations, it is not expected that we could resolve individual giant molecular clouds (GMCs) with small velocity dispersion but more likely some giant molecular associations (GMAs) with a typical velocity dispersion of a few tenths of a km s^{-1} .

We produced a combined list of cloud candidates from these four cloud-candidate lists by requiring at least one detection in the image and one detection in the spectrum. The final list of cloud candidates presented in this paper (Table 3) was obtained by requiring that each cloud line have a minimal velocity dispersion of 6 km s^{-1} and a total S/N of 6. We increased the S/N criteria to 6 in order to remove potential false detections, given that the data sample size is a few million (depending on the velocity resolution). An S/N of 5 could still return a few false detections (one per 3 million sample, on average). We note, however, that the velocity dispersion criteria and the requirement to detect the line in a pixel spectrum as well as in the image is more stringent, and that an S/N of 5 returns the same cloud candidate for our data. The minimum velocity dispersion of 6 km s^{-1} allows us to properly sample the lines, given that the data have been analyzed at a velocity resolution of at most 3 km s^{-1} .

The rather conservative approach used in selecting cloud candidates makes us worry about losing real clouds that could have been marginally detected. Indeed, by relaxing the selection criteria to an S/N greater than 3 and allowing a detection in either the spatial or velocity space, a number of cloud candidates become apparent in NGC 5846 and NGC 4636. These additional clouds seem to closely follow the filaments and ridges evident in the $\text{H}\alpha + [\text{N II}]$ image and are not randomly distributed in the field as expected from spurious signals. Although there are hints that these clouds may be real with a low-level detection, we decided not to include them in our analysis because their extent in the velocity domain was often very limited and the detection was not confirmed in the spatial plane. Deeper ALMA observations would be required to confirm a positive detection of these clouds.

The final list of clouds contains three detections for NGC 5846, two for NGC 4636, and 17 for NGC 5044. Our new data reduction and cloud selection criteria for NGC 5044 yield a lower number of cloud detections (17) when compared to the earlier published list (24) by David et al. (2014). Figure 1 shows the location of the CO clouds detected by David et al. (2014) and with our updated reduction as blue crosses and red dots, respectively. To be consistent with cloud labeling in David et al. (2014), the original cloud number sequence has been maintained. There are nine unconfirmed clouds previously listed in David et al. (2014), and two new clouds, 25 and 26, that passed our detection criteria. The vast majority of clouds in the central region are confirmed, as is the ridge of clouds extending to the northwest part of the sky. The reason for the discrepancy in CO cloud detection in NGC 5044 may be the selection criteria that we used to detect clouds. Indeed, David et al. (2014) used a lower S/N of 4 as a threshold for cloud detection in the earlier NGC 5044 reduction. To avoid false-positive detections, we set our criteria to be quite restrictive and conservative, requiring a robust S/N threshold to be met. This is supported by the fact that most of the missing clouds reside toward the edge of the primary beam extension, where the

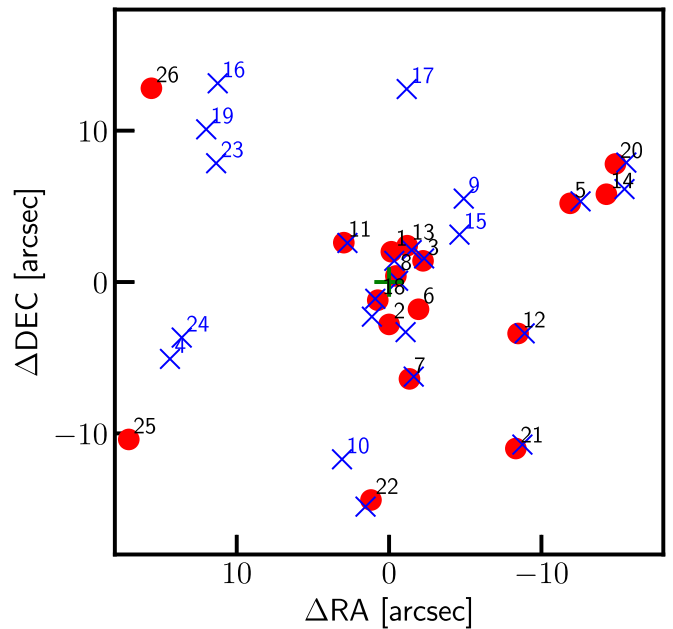


Figure 1. CO clouds detected in NGC 5044. Blue crosses and red dots show the locations of CO clouds detected by David et al. (2014) and with our updated reduction, respectively. For consistency with cloud labeling in David et al. (2014), the original cloud number sequence has been maintained. Our detection criteria did not confirm nine clouds previously listed by David et al. (2014), while two new clouds, 25 and 26, are now apparent in the field.

instrumental noise is higher. Also, some of the confirmed clouds are displaced by $\sim 1''$ when compared with the cloud locations of our new reduction. This may be due to updated housekeeping astrometry in the CASA software. The physical properties of the confirmed clouds in NGC 5044 will be discussed in the following sections, but in general terms, they are in good agreement with the results previously published by David et al. (2014).

4.1. CO Clouds in NGC 5846 and NGC 4636

Figures 2 and 3 show the distribution of the CO(2–1)-detected clouds in NGC 5846 and NGC 4636 projected against an $\text{H}\alpha + [\text{N II}]$ map (left panels) and an *HST* dust absorption map (right panels). The $\text{H}\alpha + [\text{N II}]$ images have been taken with the SOAR telescope with an average seeing of $\sim 0''.7$. The registration of the $\text{H}\alpha + [\text{N II}]$ and CO images is correct within an uncertainty of about $0''.2$ due to the astrometry in the SOAR data (Werner et al. 2014). In the figures, the optical dust maps were generated from archival *HST* data recorded with the WFPC2 in the F555W, F547M, and F814W filters.

Two of the three CO clouds detected in NGC 5846, clouds 1 and 3, are resolved in at least one direction by the 12 m array observations and extend to $1''.2$ and $2''.9$, respectively. Black and white contours outline the CO clouds and are defined as the area where the emission-line S/N is greater than 4. Cloud 2 in NGC 5846 and 1 in NGC 4636 are outside the field of view of the high-resolution *HST* dust map. These clouds are also quite close to the edge of the ALMA primary beam and were only detected when the cleaning threshold was set to about 1.5 times the rms noise; therefore, they could still be artifacts created by the “cleaning” algorithm.

Three out of five clouds detected in these two galaxies are located in a region where the $\text{H}\alpha + [\text{N II}]$ emission is relatively large, although not in the strongest emission region and not

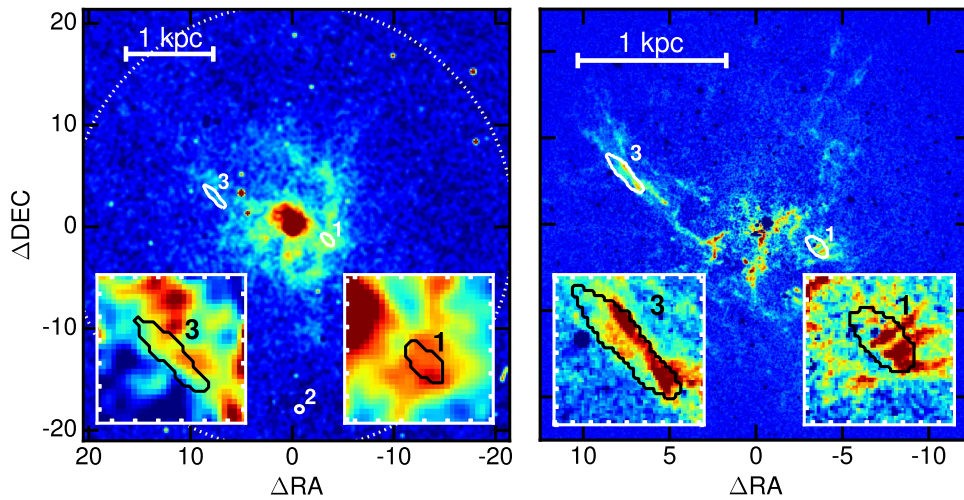


Figure 2. Images of NGC 5846 showing detected CO(2–1) clouds projected against an optical $H\alpha$ +N[II] emission image (left) and a dust starlight extinction image (right). The color sequence (blue \rightarrow green \rightarrow yellow \rightarrow red) indicates increasing $H\alpha$ +N[II] and dust. CO clouds, indicated with black (in the insert) and white contours, are defined as the area where the emission-line S/N is greater than 4. Clouds 1 and 3 are somewhat resolved and extend about $1''.2$ and $2''.9$. Note that cloud 3 (see enlarged insert) is aligned almost exactly along a dust filament and coincides with knots and filamentary structures in the $H\alpha$ +N[II] emission. Cloud 1 also coincides with $H\alpha$ +N[II] emission and dust extinction, but other similar dusty regions were not detected in CO(2–1). Cloud 2 is not associated with detectable optical emission and is out of the dust extinction map field of view. The registration of the $H\alpha$ +N[II] and CO images is correct within an uncertainty of about $0''.1$ – $0''.2$ in the astrometry in the SOAR data. The effective radius of NGC 5846 in the K band is $35''.75$. The white dashed circle in the $H\alpha$ +N[II] emission map identifies the field of view of the ALMA primary beam.

quite at the center of the galaxy. Clouds 1 and 3 in NGC 5846 are about $5''.5$ and $8''.4$ away (0.6 and 1.0 kpc) from the galaxy center, and cloud 2 in NGC 4636 is about $2''.6$ away from the central nucleus (200 pc).

The *HST* images have a $25''$ field of view, and only central cloud contours are visible. There is a good correlation between the cloud position and the dust absorption in both NGC 5846 and NGC 4636, although several heavily obscured parts of each galaxy do not show a CO(2–1) surface brightness large enough to be detected in our data.

In NGC 5846, cloud 3 is aligned almost exactly along a dust filament, while cloud 1 also coincides with small dust extinction structures (about $0''.5/\sim 60$ pc wide), but other similar dusty regions were not detected in CO(2–1). Cloud 2 in NGC 4636 is located in the same area of one of the most obscured regions of NGC 4636. Both clouds in NGC 4636 are not resolved by these observations, implying an angular size $\leq 0''.7$ (~ 50 pc).

Figure 4 shows the spectra of the five CO(2–1) clouds detected. For the two resolved clouds (clouds 1 and 3 in NGC 5846), the spectra have been obtained by summing the signal from the pixels of each cloud (contiguous pixels with an S/N greater than 3 times the rms noise within the velocity range of the emission line). For unresolved clouds, the spectra are taken from the pixels with the largest S/N within the velocity range of the emission line.

A Gaussian fit to the emission line is presented as a red line in Figure 4. Cloud 1 in NGC 4636 has a double-peaked spectrum that cannot be fitted with a single Gaussian curve. The spectrum could be interpreted as generated by two distinct clouds that have similar projected positions on the sky but with a differential peak-to-peak velocity of ~ 40 km s $^{-1}$. Unfortunately, since the cloud is not resolved by our current ALMA configuration, we cannot quantify its kinematics properties, including its gas velocity dispersion.

4.2. CO Clouds in NGC 5044

Our new reduction of the Cycle 0 ALMA data on NGC 5044 confirmed the detection of 17 CO(2–1) clouds. Figure 5

shows the distribution of the detected clouds overlapped on a false-color $H\alpha$ +N[II] map (left panel) and an *HST* dust absorption map (right panel). Most of the clouds in NGC 5044 are located within a radius of approximately $5''$ around the center of the galaxy. In Figure 5, unresolved clouds are identified with an ellipse roughly the size of the beam, while contours, at 4 times the rms noise level, are used to represent the extended molecular clouds/associations. With a resolution of $2''.0 \times 1''.4$, only four clouds are resolved by these observations: clouds 8, 13, 14, and 18.

The *HST* dust extinction map presents several compact knotty features in its central region. All of the central CO clouds lie on top of these strong dust absorption features, with the larger (resolved) clouds encompassing few clumps of dust. In the central $5'' \times 5''$, there is a good correlation between dust features and molecular clouds. However, more distant clouds in the *HST* field of view (clouds 7, 12, and 21) are not correlated with dust absorption.

The $H\alpha$ +N[II] emission map shows a very peaked central emission with the addition of diffuse and filamentary structures that extend up to $30''$ from the galaxy center. From the total of 17 clouds, 12 are located where the $H\alpha$ +N[II] emission is fairly large, and eight of these clouds are within $4''.6$ from the center of the galaxy. In this central $\sim 5''$ region, the molecular clouds are located where the $H\alpha$ +N[II] emission is strongest, broadly providing a correlation between optical line emission and CO gas. On the other hand, the spatial distribution of the eight central clouds does not rigorously follow the morphology of the $H\alpha$ +N[II] emission (see insert in Figure 5). Given the weak angular resolution of NGC 5044 CO(2–1) observation, we cannot exclude that some better correlation exists with a subset of clouds. The remaining five clouds (5, 14, 20, 25, and 26) are located far from the center, between $12''$ and $22''$. Clouds 25 and 26 were only detected with the cleaning threshold set to 1.5 times the rms noise, so they could be artifacts created by the “cleaning” algorithm.

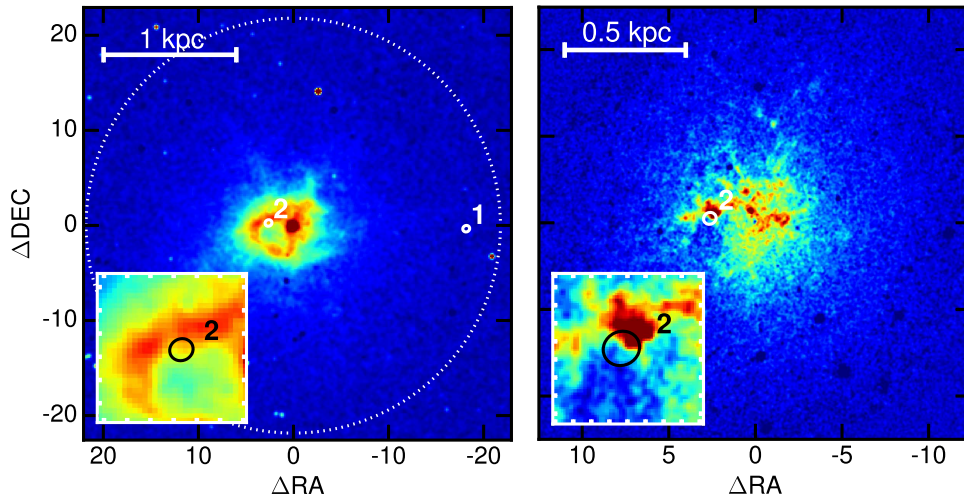


Figure 3. CO(2–1) clouds in NGC 4636 projected against the galaxy images (same as Figure 2). Cloud 1 is not associated with detectable optical emission and is out of the dust extinction map field of view, while cloud 2 is centered on a dust absorption knot and aligned with a ridge in the optical line emission map. None of the clouds in NGC 4636 are resolved. The effective radius of NGC 4636 in the K band is $56''.29$. The white dashed circle in the $H\alpha+[N\text{ II}]$ emission map identifies the field of view of the ALMA primary beam.

Figure 6 shows the spectra of the 17 CO(2–1) clouds detected. For the four resolved clouds, the spectra have been obtained using a similar procedure to that described earlier for NGC 5846. Also, for unresolved clouds, the spectra are taken from the pixels with the largest S/N within the velocity range of the emission line. A Gaussian fit to the emission line is presented as a red line in Figure 6. The spectra are displayed with a bin size in velocity of 10 km s^{-1} . Since cloud 22 has a large velocity dispersion, its spectrum is presented with a velocity bin size of 50 km s^{-1} .

5. Analysis

Table 1 contains the basic parameters of the detected clouds, including the average velocity, velocity dispersion, and total flux (corrected from the primary beam effect), as well as the corresponding molecular mass and cloud dimensions. The velocity and velocity dispersion have been obtained by fitting a Gaussian on the spectra of each cloud. For each cloud, the flux has been obtained by summing the emission of the spectra described previously and ranges from 70 to $3000\text{ mJy km s}^{-1}$. The molecular mass of each cloud is computed by using (Bolatto et al. 2013)

$$M_{\text{mol}} = 1.05 \times 10^4 \left(\frac{X_{\text{CO}}}{2 \times 10^{20}} \right) \frac{S_{\text{CO}} \Delta \nu D_L^2}{(1+z)} M_{\odot}, \quad (1)$$

where $S_{\text{CO}} \Delta \nu$ is the integrated line flux density in Jy km s^{-1} in the ground rotational transition $J = 1 \rightarrow 0$, D_L is the luminosity distance to the source in Mpc, and z is the redshift. Throughout the paper, we use the reference conversion factor $X_{\text{CO}} = 2 \times 10^{20} \text{ cm}^{-2} (\text{K km s}^{-1})^{-1}$ to evaluate the molecular gas mass in each detected cloud.

To convert the CO(2–1) flux into CO(1–0) flux, we assume that the CO(2–1)-to-CO(1–0) temperature brightness ratio is 0.8, as found by Braine & Combes (1992), so that the flux density ratio is 3.2 due to the frequency factor (David et al. 2014). The ACA data do not exhibit any detection, and the clouds detected in the 12 m array data are below the sensitivity of the ACA data. Cloud 3 of NGC 5846 has a peak flux density of 10 mJy in a 10 km s^{-1} bin that only represents a 2.5 rms

noise signal at the center of the ACA observation. Cloud 1 of NGC 4636 has a peak flux density of about 5.5 mJy in a 10 km s^{-1} bin that only represents a 2.3 rms noise signal at the center of the ACA observation. Using the known location in space and velocity of cloud 3 of NGC 5846, we measure a signal with a flux density of $8.1 \pm 2.0\text{ mJy beam}^{-1}$ by increasing the bin size to 50 km s^{-1} . However, we detect other sources as well. Given the large amount of data, we expect several spurious detections at 4 times the rms noise. We verify that the ACA data are consistent with the 12 m data, but the ACA data alone are not sufficient to detect even cloud 3 of NGC 5846.

Using the reference X_{CO} factor, the derived molecular masses of the detected clouds vary from 1×10^5 to $9 \times 10^6 M_{\odot}$. For clouds that have been resolved along at least one of their dimensions by ALMA observations, we used the *imfit* function from the CASA package to calculate their size. For simplicity, we refer to these clouds as resolved or extended, even if one of their dimensions is smaller than the beam. The *imfit* function fits an elliptical Gaussian component and returns the size of the major/minor axis and position angle, as well as their associated errors (Condon 1997). This model might not be the best match for the molecular cloud shape; however, our measured residuals are consistent with pure noise, which might be due to the fact that none of the clouds are very well resolved. The values quoted in Table 3 correspond to the size deconvolved from the beam, except for cloud 3 of NGC 5846, because its fitted minor axis is too close to the beam size (within the beam size considering the uncertainties), so the size of the minor axis cannot be deconvolved.

Clouds 1 and 3 in NGC 5846 measure $1''.2$ and $2''.9$ (major axis), respectively; these scales correspond to a physical size of 143 and 346 pc. Clouds 8, 13, 14, and 18 measure $3''.9$, $3''.8$, $3''.1$, and $1''.9$ (major axis), corresponding to 590, 575, 469, and 287 pc. It is not clear whether these clouds are really contiguous or formed of several smaller clouds. Unresolved clouds are constrained to have a physical size smaller than 82, 50, and 300 pc for NGC 5846, NGC 4636, and NGC 5044, respectively, given the angular resolution of our ALMA observations and the assumed distance of these galaxies.

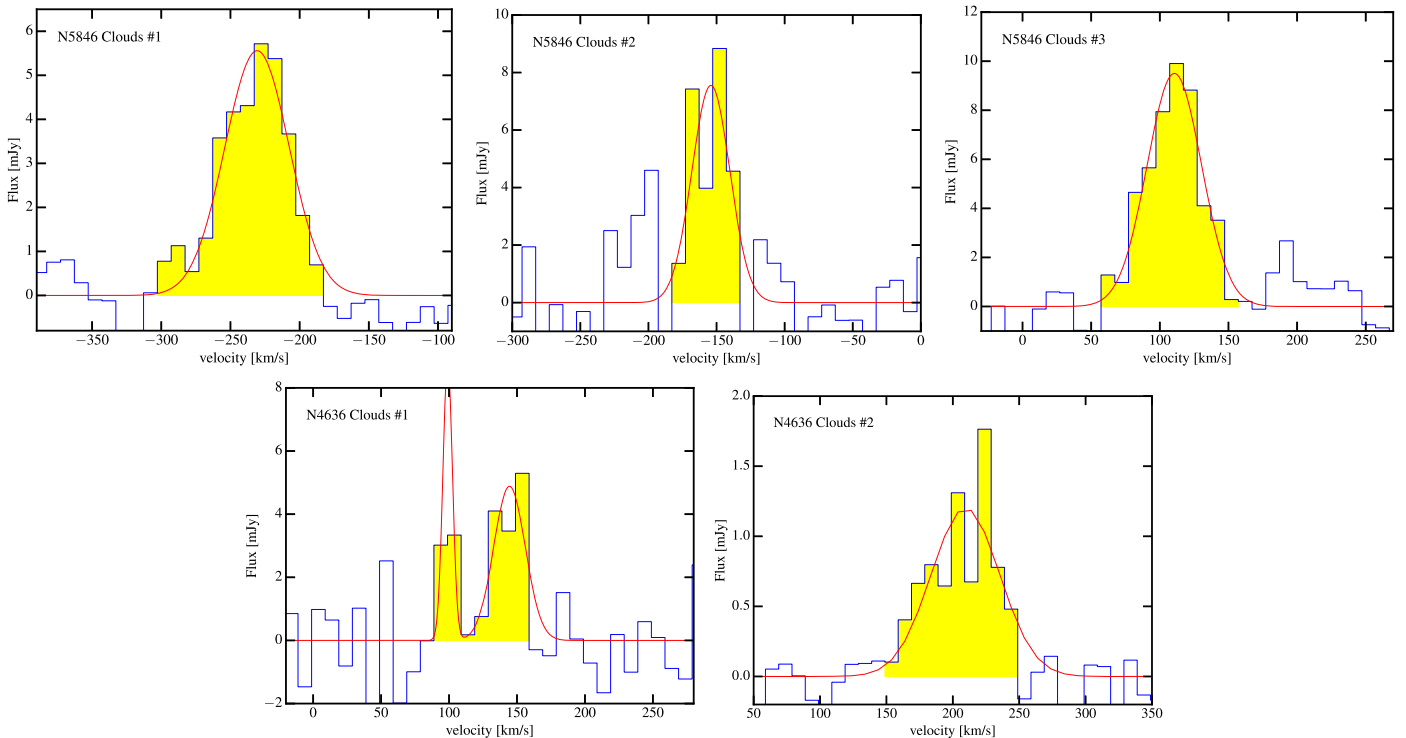


Figure 4. Spectra of the five clouds detected in ALMA CO(2–1) images of NGC 5846 (top) and NGC 4636 (bottom), with a Gaussian fit to the emission line (red). The cloud 1 and 3 spectra of NGC 5846 were computed, respectively, over 144 and 221 pixels covering a solid angle of 1.4 and 2.2 arcsec² (contiguous pixels with S/N greater than 3), whereas, since the other clouds are unresolved, the spectra correspond to the pixel with the largest S/N.

The larger surface brightness and size of clouds 1 and 3 in NGC 5846 and clouds 8, 13, 14, and 18 in NGC 5044 allow us to map out their properties. Figures 7 and 8 present the surface brightness, velocity, and velocity dispersion maps of the NGC 5846 and NGC 5044 clouds. The surface brightness has been calculated by integrating between -3σ and $+3\sigma$ (the velocity dispersion σ is fitted on the spectra) of the spectra of each pixel (-303 to -163 and 37 to 157 km s⁻¹ for clouds 1 and 3 of NGC 5846, for instance). The velocity and velocity dispersion have been calculated by fitting a Gaussian to each pixel spectra. The elongation and potential bimodality of the surface brightness of cloud 3 of NGC 5846 could indicate that it might be composed of two nearby (in projection) clouds. The velocity varies slowly along the major axis of the cloud from about 100 to 120 km s⁻¹ and could either substantiate the existence of two clouds or indicate some rotation of a larger cloud. The velocity dispersion of cloud 3 is fairly uniform between 17 and 21 km s⁻¹, given the uncertainty of about 5 km s⁻¹, and only seems to increase to 25 km s⁻¹ at the edges of the major axis. Our observation angular resolution is not quite good enough to distinguish a two- or one-cloud scenario.

Cloud 1 of NGC 5846 has a more unimodal surface brightness shape, and its surface brightness peaks roughly at its center. The velocity is varying across the cloud with $\Delta v = 25$ km s⁻¹, which, given the uncertainty of 4 km s⁻¹, is statistically significant. The shape of the velocity distribution is compatible with tidal disruption. The velocity dispersion varies quite significantly within the cloud, from 15 to 32 km s⁻¹ (error estimate is about 4 km s⁻¹).

All resolved clouds of NGC 5044 are quite unimodal, and all clouds but cloud 18 are fairly elongated. They have a much larger velocity spread along their major axis ($\Delta v \sim$

60–80 km s⁻¹) compared to the resolved clouds in NGC 5846 ($\Delta v \sim 20$ –30 km s⁻¹).

5.1. Continuum

All three galaxies analyzed in this paper have a detected continuum around the CO(2–1) line. The measured continuum for NGC 4636, NGC 5846, and NGC 5044 is, respectively, 0.4 ± 0.1 , 10.63 ± 0.03 , and 52.8 ± 1.5 mJy. Each continuum is detected as a point source with a size limited by the point spread function (PSF) of the observation (about 0''.6 for NGC 4636 and NGC 5846 and 1''.7 for NGC 5044, corresponding to 51 and 255 pc).

An absorption feature seen in the NGC 5044 continuum spectrum of the central continuum source shows that the emission must be very compact and probably arises from the AGN (David et al. 2014). We have not detected any absorption features associated with the central continuum source in NGC 5846 or NGC 4636.

Using FIR data from *Spitzer* and *Herschel*, when available, as well as radio data, it is possible to fit for the FIR and radio spectra to weight the contribution of each to the continuum at 230 GHz as seen by ALMA. FIR data from *Spitzer* and *Herschel* were taken from Temi et al. (2009) and Amblard et al. (2014), respectively; in these data, all three galaxies are unresolved. The radio data were taken from a variety of observations by Vollmer et al. (2004), Filho et al. (2004), Nagar et al. (2005), and Giacintucci et al. (2011); the fluxes were corrected assuming a uniform brightness when the scale at which they were measured differed greatly from that of the ALMA PSF.

Figure 9 summarizes the observations between 10 μ m (30 THz) and 1 m (300 MHz) for our three galaxies. NGC 4636 has the best coverage in the FIR with data from *Herschel*/SPIRE. The fit of an FIR modified blackbody

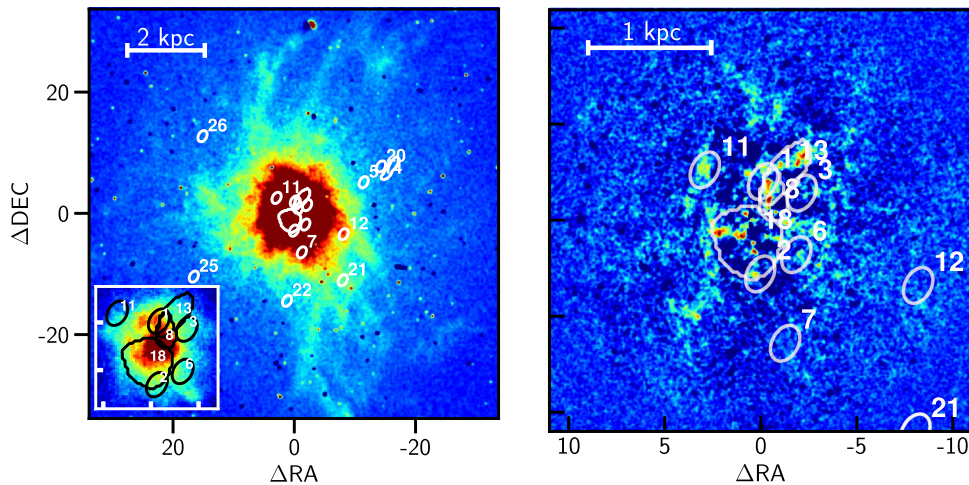


Figure 5. Images of NGC 5044 showing detected CO(2–1) clouds projected against an optical $H\alpha$ + $[N\ II]$ emission image (left) and a dust starlight extinction image (right). The color scheme of the background images and cloud contours are as described in the caption of Figure 2. The revised data reduction accounts for 17 CO clouds in the central ~ 6 kpc. Cloud labeling reflects the original sequence presented in David et al. (2014). The combination of newer pipeline software and a more stringent set of criteria for cloud detection did not confirm a few CO clouds originally listed in David et al. (2014). Clouds 8, 13, 14, and 18 are resolved. Three of the four resolved clouds reside in the central ~ 2 kpc region (see enlarged insert) and overlap with several knots in the dust extinction maps, as well as with the $H\alpha$ + $[N\ II]$ emission in the galaxy center. The registration of the $H\alpha$ + $[N\ II]$ and CO images is correct within an uncertainty of about $0''.1$ – $0''.2$ in the astrometry in the SOAR data.

spectrum (emissivity $\beta = 1.5$) returns a temperature of 31.8 ± 0.9 , 30.0 ± 1.1 , and 30.7 ± 1.2 K and an FIR luminosity of $10^{7.91 \pm 0.02}$, $10^{8.13 \pm 0.03}$, and $10^{8.71 \pm 0.03} L_{\odot}$ for NGC 4636, NGC 5846, and NGC 5044, respectively. The faint NGC 4636 ALMA continuum is in good agreement with the expected emission from cold dust, which would indicate that the dust content of NGC 4636 is fairly centrally located. The stronger continuum from NGC 5846 and NGC 5044 is an order of magnitude larger than the expected emission from cold dust or synchrotron. This strong continuum could be due to free–free emission from H II regions, which can dominate in the 30–200 GHz range. However, these results are somewhat weakened by the fact that some of these observations were performed at difference scales. Given that the FIR fluxes were measured on a larger scale than the ALMA fluxes, cold dust emission could not contribute more to the ALMA fluxes for NGC 5846 and NGC 5044, but the synchrotron contribution could be larger or lower depending on the model adopted to match the observed scales. It is also not possible to exclude that the NGC 4636 ALMA flux could be a combination of synchrotron and dust emission, even if it matches the cold dust spectral energy density (SED). New radio observations matching the ALMA PSF would allow us to improve this analysis.

5.2. Kinematics Interpretation

Clouds 1 and 3 of NGC 5846 are resolved and have an average radius ($r_c = \sqrt{\sigma_{\text{maj}}\sigma_{\text{min}}}$) of $0''.21 \pm 0''.11$ and $0''.61 \pm 0''.04$, respectively (see Table 4). For these clouds, we calculate the surface mass density that is, respectively, 460 ± 332 and $39 \pm 4 M_{\odot} \text{pc}^{-2}$, and the n_{H_2} volume densities are, respectively, 274 ± 240 and $8.0 \pm 1.0 \text{cm}^{-3}$. NGC 5044 clouds have an average radius between 79 and 139 pc, a surface mass density of 56 ± 24 , 75 ± 56 , 76 ± 43 , and $476 \pm 214 M_{\odot} \text{pc}^{-2}$, and an n_{H_2} volume density of 6 ± 3 , 11 ± 10 , 10 ± 7 , and $89 \pm 49 \text{cm}^{-3}$ for clouds 8, 13, 14, and 18, respectively. The large uncertainty of these values is due to the fact that the minor axis of all the clouds is very close to the size of the beam; the deconvolved value of the minor axis (σ_{min}) is therefore very small and has a large relative uncertainty. The

lower uncertainty on cloud 3 is due to the fact that we are using the convolved value of its dimension, since we could not deconvolve the value of its minor axis.

To derive whether these molecular associations are gravitationally bounded, we can calculate the virial parameters from Bertoldi & McKee (1992):

$$\alpha = \frac{5\sigma^2 R}{GM}, \quad (2)$$

A virial parameter of ~ 1 indicates that a cloud is gravitationally bound, while a virial parameter $\gg 1$ indicates that a cloud is unbound or pressure-bound. All of the detected and resolved clouds have a virial parameter much $\gg 1$ (see Table 2), although with large uncertainties (due to large errors in the cloud radii). Deeper observations with a better PSF could allow us to more properly resolve each clump and potentially detect subcomponents with thinner CO lines. These subcomponents could have smaller virial parameters. Indeed, the large virial parameters might indicate that the clouds in NGC 5846 and NGC 5044 are unbound giant molecular associations drifting in the turbulent velocity field (dominated by the large eddies at kpc scale) that may disperse in a relatively short timescale $r_c/\sigma \approx 1$ – 10 Myr. Alternatively, the large CO line widths may arise in molecular gas flowing out from the cloud surfaces due to heating by the local hot gas atmosphere. Deeper observations with a smaller PSF are needed to better characterize the CO clumps detected in these observations.

6. Discussion

Our new observations and detection of CO-emitting clouds in NGC 5846 and NGC 4636 confirm the presence of molecular gas in group-centered galaxies in the form of compact clouds. A diffuse CO component, if present, has not been detected by our ACA observations in these two galaxies. Previous attempts at detecting diffuse molecular gas with single-dish observations have failed as well (Combes, IRAM observations).

Because of the angular sensitivity of interferometric measurements, ALMA observations are sensitive to emission

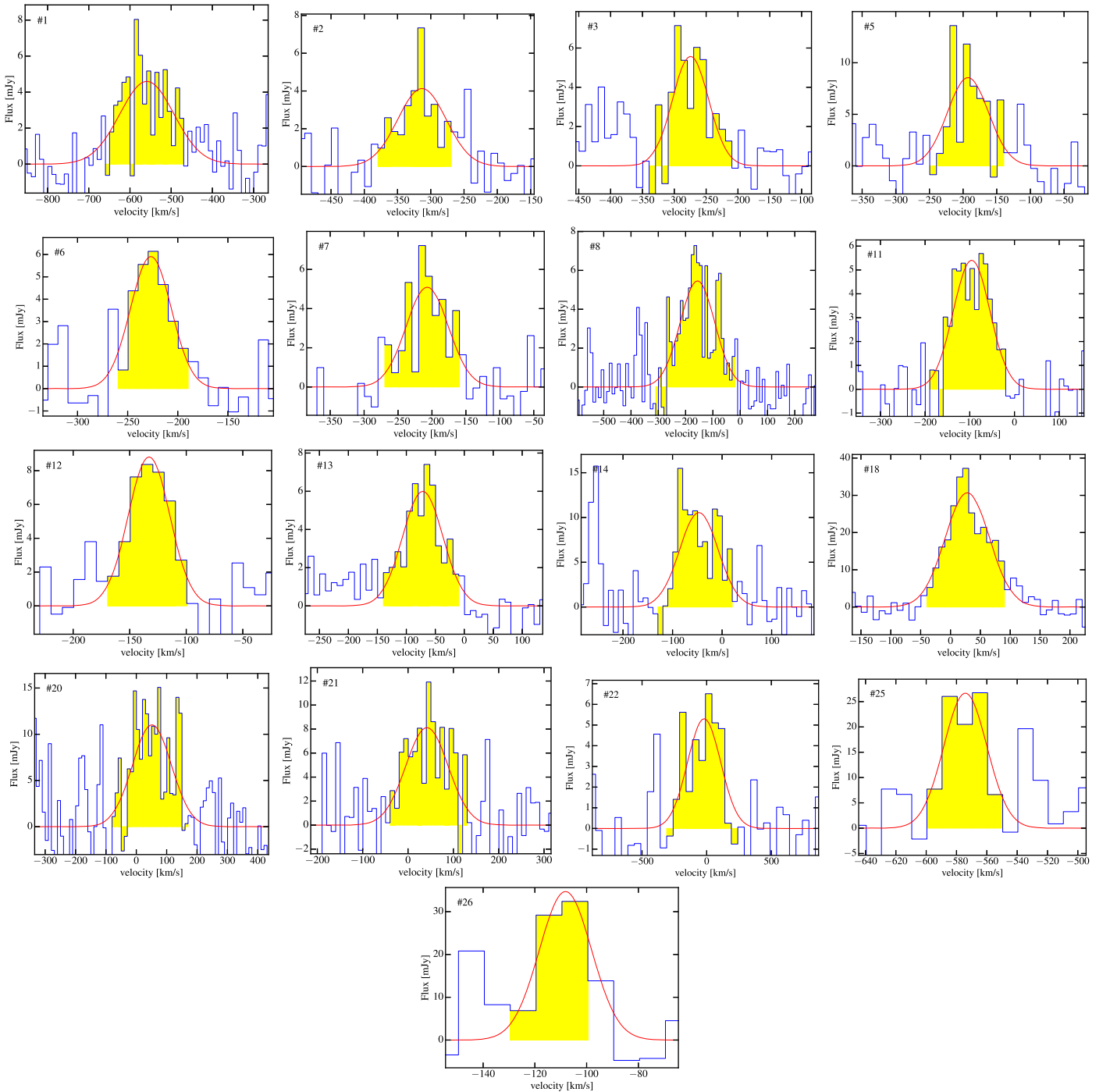


Figure 6. CO(2–1) spectra of the 17 clouds detected in NGC 5044, along with a Gaussian fit to the emission line (red curve). The velocity bin size is 10 km s^{-1} , except for cloud 22, where the bin size is 50 km s^{-1} .

in a selected range of angular scales. At the scale distance of galaxy groups, ALMA observations preferentially detect individual clouds, which may comprise a small fraction of the total molecular mass. In more distant clusters, where the ALMA beam size is of the order of a few kpc, the maximum recoverable size becomes a good match for detecting the diffuse emission (David et al. 2017).

It is worth noting that the molecular gas masses reported in Table 3 have been evaluated assuming the conversion between CO luminosity and H_2 mass derived for our Galaxy or other normal star-forming galaxies. However, such a conversion

factor may not be appropriate for massive elliptical galaxies at the center of groups and clusters (Lim et al. 2017 and references therein). The environment in which the molecular gas is immersed in massive ellipticals strongly constrains and defines the physical parameters of the molecular gas, and it differs substantially from the surrounding ambient of Galactic GMCs. The Galactic X_{CO} may overpredict the mass of CO clouds in this very different group environment where the CO line emissivity may be unusually large. Using ALMA observations of CO(3–2) and $^{13}\text{CO}(3–2)$ in the brightest cluster galaxy of RXJ0821+0752, Vantyghem et al. (2017) estimated

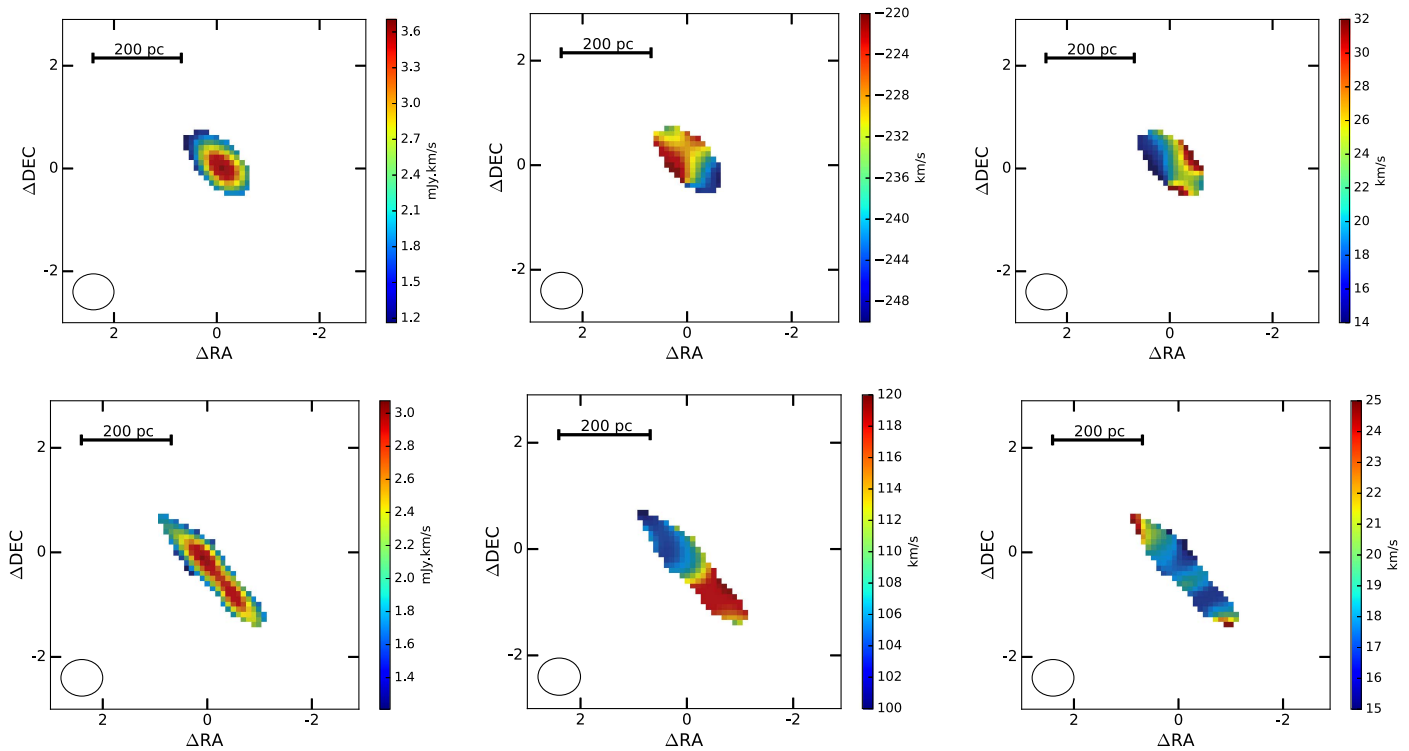


Figure 7. Flux (left), velocity (center), and velocity dispersion (right) in clouds 1 (top) and 3 (bottom) of NGC 5846. The flux image has been calculated by integrating the signal from -303 to -163 and 37 to 157 km s^{-1} , respectively; flux errors are typically about 0.3 mJy km s^{-1} . Velocity and velocity dispersion have been obtained by fitting the emission line and have a typical respective uncertainty of 4 and 5 km s^{-1} . The ellipse in the bottom left corner represents the ALMA beam size.

that the galactic X_{CO} factor overestimates the true molecular mass by a factor of two.

There is mounting evidence that the molecular gas in these systems cooled from the hot interstellar or intragroup medium (e.g., Hogan et al. 2017; Pulido et al. 2017 and references therein).

A remarkable observational result is the cospatiality among the different gas phases that extend to the observed filamentary structures of each gaseous component. For instance, for the three galaxies presented here, the X-ray emission is highly cospatial with the optical, infrared, and radio emission of cold/warm gas (e.g., Werner et al. 2014). The [C II] emission, thought to originate in warm gas that roughly moves with the hot gas, correlates well with the $\text{H}\alpha + [\text{N II}]$ emission, and in all three galaxies, the [C II]/ $\text{H}\alpha + [\text{N II}]$ ratio remains relatively constant with a total luminosity ratio ~ 0.6 (Werner et al. 2014), corroborating the scenario of in situ gas condensation via nonlinear thermal instability. Dust absorption features in the optical *HST* images show a good correlation with the central $\text{H}\alpha + [\text{N II}]$ emission and filamentary structures (see Figures 2 and 3).

In addition, multiwavelength observations indicate that the presence of a multiphase ISM strongly correlates with the hot atmosphere properties, such as short cooling time ($t_{\text{cool}} \lesssim 3 \times 10^8$ yr), low entropy parameter ($kT/n^{2/3} \lesssim 15$ keV cm^2), small cooling time-to-dynamical time ratio ($t_{\text{cool}}/t_{\text{dyn}} \lesssim 20$), and $t_{\text{cool}}/t_{\text{eddy}} \approx 1$. Early 2D hydrodynamic simulations of AGN-heated galaxy group atmospheres (Brighenti & Mathews 2002) suggested that spatially distributed cooling occurs in localized compressed regions, where nonlinear density perturbations cool rapidly to $T \lesssim 5 \times 10^4$ K. In recent years, much

progress has been made in our understanding of the heating/cooling cycle in galaxies and clusters (Revaz et al. 2008; Gaspari et al. 2012, 2013, 2017b, 2017a; McCourt et al. 2012; Sharma et al. 2012; Li & Bryan 2014; Brighenti et al. 2015; Li et al. 2015; Valentini & Brighenti 2015; Voit et al. 2017). These studies have shown that cooling perturbations can be generated by several sources, like turbulence (e.g., Gaspari et al. 2012), AGN outflows (e.g., Gaspari et al. 2011), or buoyant cavities (e.g., Brighenti et al. 2015). The latter two mechanisms are particularly effective in stimulating cooling because they cause some of the low-entropy central gas to be transported to larger radii (albeit only along a preferential direction), where the dynamical time is larger (see also McNamara et al. 2016).

However, a general prediction for these cooling scenarios is that the cold gas should be dust-poor (e.g., Valentini & Brighenti 2015 and references therein), although additional physics (such as dust growth by accretion of gas-phase metals in the cold gas) may alter this outcome (Hirashita & Nozawa 2017). This prediction seems to be confirmed by our observation, where many CO clouds do not extinct background starlight, especially in NGC 5044; although, given their small angular sizes, dusty clouds may not obscure much starlight. Thus, the exact alignment of NGC 5846 clouds 1 and 3 in Figure 2 with the dust suggests a further mechanism to form cold gas.

They could have only recently formed from relatively dust-rich gas produced by mixing dusty stellar mass loss or dusty warm gas originally present in the center of the galaxy and uplifted by the AGN outburst with hot ISM. Dust-enhanced cooling can easily cool hot gas on timescales less than the local freefall time (Mathews & Brighenti 2003).

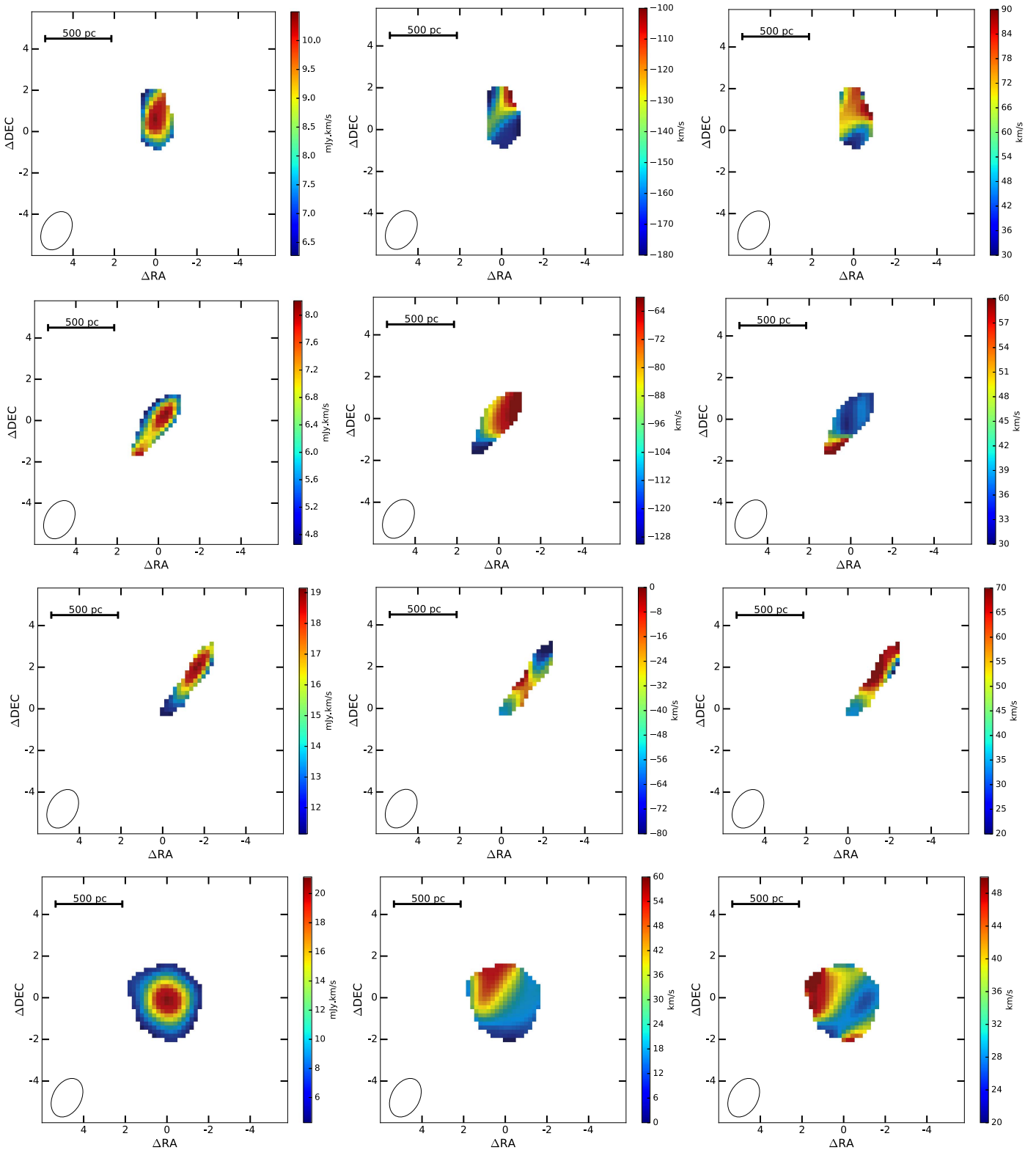


Figure 8. Flux (left), velocity (center), and velocity dispersion (right) in clouds 8, 13, 14, and 18 of NGC 5044. The flux image has been calculated by integrating the signal 3σ around the peak, and flux errors are typically about 1 mJy km s^{-1} (except for cloud 13, where it is 4 mJy km s^{-1}). Velocity and velocity dispersion have been obtained by fitting the emission line and have a typical uncertainty 8 km s^{-1} . The ellipse in the bottom left corner represents the ALMA beam size.

Another possible origin for orbiting dusty molecular clouds is direct acceleration of molecular gas present in the central region. However, as discussed by McNamara et al. (2016) and references therein, it is unclear how low-density jets or

buoyant cavities can drag very dense and compact clouds to heights of several kpc.

More distant CO clouds, like cloud 2 in NGC 5846, not associated with gas having an enhanced dust/gas ratio, are

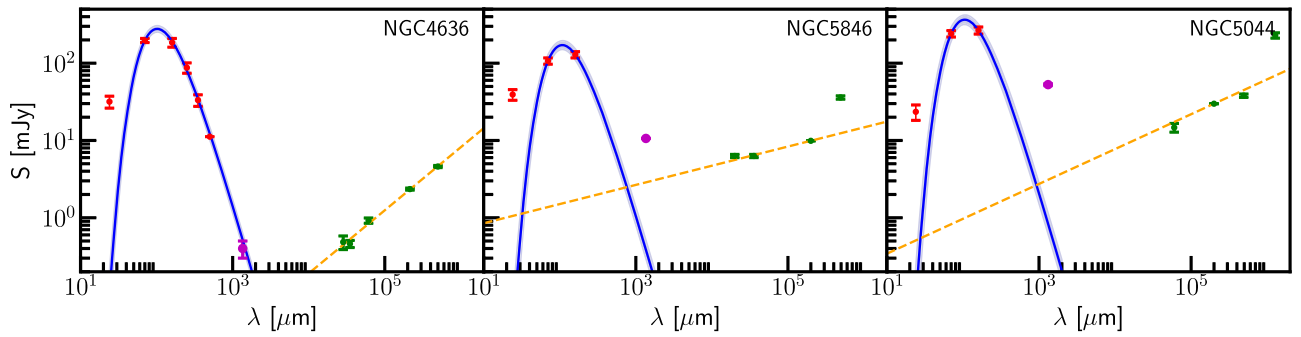


Figure 9. FIR to radio spectra of NGC 4636 (left), NGC 5846 (center), and NGC 5044 (right). Red circles represent data from *Spitzer*/MIPS and *Herschel*/SPIRE (NGC 4636), green circles represent radio measurements, and magenta circles represent our ALMA continuum measurements. The blue line is a modified blackbody (emissivity $\beta = 1.5$) fit to the data in the 70–500 μm range, and the light blue shading represents its uncertainty. The orange dashed line is a fit to the radio data by a power-law spectrum.

Table 4

Cloud Radius, Surface Mass Density, Volume Density, and Virial Factor for the Two Resolved Clouds of NGC 5846 and the Four Resolved Clouds of NGC 5044

ID	r_c (pc)	Σ ($M_\odot \text{pc}^{-2}$)	n_{H_2} (cm^{-3})	α
NGC 5846				
1	24.8 ± 12.6	460.2 ± 331.9	274.2 ± 241.7	18.0 ± 9.4
3	72.2 ± 4.3	39.1 ± 4.1	8.0 ± 1.0	53.0 ± 7.7
NGC 5044				
8	139.0 ± 41.8	55.9 ± 24.3	5.9 ± 3.1	283.8 ± 96.9
13	104.8 ± 54.2	75.4 ± 55.6	10.6 ± 9.6	89.2 ± 52.6
14	113.1 ± 41.4	76.4 ± 43.4	10.0 ± 6.8	66.8 ± 35.2
18	79.2 ± 25.1	476.1 ± 214.2	88.9 ± 48.9	14.1 ± 4.6

thought to originate from cooling in the wakes beneath buoyant X-ray cavities where compressions stimulate significant large-scale, coherent radiative cooling (Brighenti et al. 2015; Valentini & Brighenti 2015).

The tight spatial correlation between the soft X-ray and warm gas emission (Figure 10), together with the cold molecular gas, is an important clue that the multiphase gas arises from the top-down nonlinear condensation process (Gaspari et al. 2017a), i.e., cascading from the turbulent hot plasma to warm filaments and the molecular clouds at the overdensity peaks. The high-resolution 3D simulations in Gaspari et al. (2017a, 2017b) allow a quantitative comparison with the observations presented here. Gaspari et al. (2017b, 2017a) showed that the cold clouds often agglomerate in giant molecular associations (sometimes in projection) that are not virialized but rather characterized by significant velocity dispersion (and thus virial parameter $\alpha \gg 1$). Typical properties of simulated clouds (related to the high-end tail of the molecular gas distribution) are masses in the range 10^4 – $10^6 M_\odot$ and effective radii 50–250 pc, which are well consistent with the observational data. The simulations also predict several smaller and less massive clouds, which cannot be detected by our observations.

Analysis of the kinematics of the multiphase gas in long-term AGN jet feedback simulation runs (Gaspari et al. 2017a) reveals that warm and cold gas are—as ensemble—robust kinematic tracers of the turbulent hot gas. This is substantiated by multiwavelength observations of NGC 5044. The ensemble velocity dispersion for NGC 5044 molecular clouds (which can be approximated via the rms of the velocity offsets; Table 3) is

$\sigma_{v,\text{los,ens}} \simeq 177 \text{ km s}^{-1}$. The velocity dispersion from $\text{H}\alpha + [\text{N II}]$ data results in 190 km s^{-1} (Gaspari et al. 2017a). The two are comparable (errors are $\lesssim 10 \text{ km s}^{-1}$) and very similar to the hot plasma value of 172 km s^{-1} (Ogorzalek et al. 2017). Unfortunately, for NGC 4636 and NGC 5846, the small number of clouds detected prevents a similar analysis. Gaspari et al. (2017a) runs also show that, due to the turbulence cascade ($\sigma_v \propto l^{1/3}$), the small-scale structures typically have low velocity dispersion ($< 100 \text{ km s}^{-1}$) but large velocity shift, up to several 100 km s^{-1} , in agreement with our observational findings (Sections 4–5 and Table 3).

Overall, the consistent results between the numerical predictions and the observational findings—e.g., the cospatiality among the soft X-ray, optical/IR, and radio structures; the correlation with short plasma cooling times; the large virial parameter; the masses and radii of the clouds; the tightly linked ensemble kinematics among all of the phases (X-ray, $\text{H}\alpha + [\text{N II}]$, $[\text{C II}]$, CO); and the cloud σ_v tracing the turbulent cascade—all corroborate the important role that the top-down condensation cascade and related CCA play in shaping the multiphase halos of massive galaxies, groups, and clusters.

The broad CO line widths of the molecular clouds in these galaxies, which would imply that they are unbound systems, are of particular interest. The large CO line widths may arise in gas flowing out from cloud surfaces due to heating by the local hot gas atmosphere. Broad, rather symmetric CO line profiles are formed by the combined emission from outflows on both the near and far cloud surfaces. Fast CO outflows also guarantee that CO lines are absorbed locally; Doppler-shifted CO line radiation from distant surfaces will not be absorbed. Furthermore, extreme CO outflow velocity gradients will sharply reduce optical depths in all CO lines, and CO line emissivities may be greatly increased by collisional excitation at the relatively high temperature required to drive the observed expansion velocities. Future ALMA observations of CO at higher J transitions and proper knowledge of excitation mechanisms would provide a better characterization of the physical properties of the molecular gas and the inferred gas mass.

7. Conclusions

We have presented new CO(2–1) ALMA observations of two group-centered elliptical galaxies, NGC 5846 and NGC 4636. With the addition of the revised Cycle 0 observations of NGC 5044, we have confirmation that CO

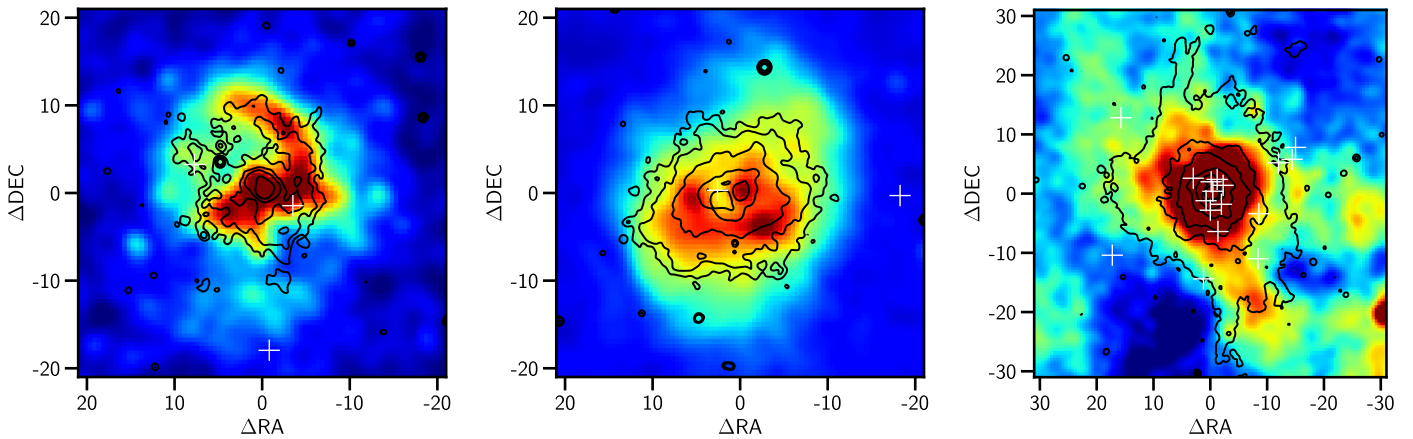


Figure 10. *Chandra* images of NGC 5846, NGC 4636, and NGC 5044 with superimposed contours of their respective $H\alpha+[N II]$ emission. An excellent correlation is apparent in the central region, as well as in the extended filamentary structures of the three galaxies. White crosses mark the detected CO cloud positions.

molecular clouds are common features in these massive ellipticals. Our main results are summarized as follows:

1. The off-center orbiting clouds exhibit CO line widths that are $\gtrsim 10$ times broader than those of Galactic molecular clouds. The associated total molecular mass ranges from $2.6 \times 10^5 M_\odot$ in NGC 4636 to $6.1 \times 10^7 M_\odot$ in NGC 5044. These masses have been estimated assuming the CO-to- H_2 conversion factor calibrated for the Milky Way and nearby spiral galaxies. Since significant deviations from the Galactic X_{CO} are observed in other galaxies (Vantyghem et al. 2017), it is expected that the presented molecular masses are overestimated. A diffuse CO component, if present, has not been detected at the sensitivity level of our ACA observations in NGC 5846 and NGC 4636. It is worth noting that, given the angular sensitivity of interferometric measurements, ALMA observations at a distance scale of local groups preferentially detect individual clouds, which may account for a small fraction of the total molecular mass.
2. The origin of the detected molecular features is still uncertain, but there is evidence that the molecular gas has cooled from the hot gas. The observed spatial and kinematical correlation among the different phases—hot (soft X-ray), warm ($H\alpha$), cold ($[C II]$), and molecular (CO)—of the multiphase gas in the atmosphere of these galaxies supports the scenario of in situ condensation, as opposed to gas stripping from merging galaxies. Also, the hot atmosphere properties—short cooling time, low entropy parameter, and small cooling time-to-dynamical/eddy time ratio—are consistent with the necessary conditions to promote gas cooling via thermal instabilities, as predicted by hydrodynamic simulations. The central CO clouds in strong spatial correlation with dust (e.g., clouds 1 and 3 in NGC 5846) may have recently formed and cooled from the hot gas phase via dust-enhanced cooling. The global condensation mechanism can be triggered via nonlinear perturbations generated in the chaotic turbulent velocity field or during the bubble uplift.
3. The large virial parameter of the molecular structures, their large CO(2–1) line widths, and correlation with the warm/hot phase kinematics provide evidence that they are unbound giant molecular associations drifting in the turbulent field, consistent with the numerical predictions of the CCA process. Alternatively, the observed large CO line widths may be generated by molecular gas flowing

out from cloud surfaces due to heating by the local hot gas atmosphere.

Despite the uncertainties listed above, we expect the surfaces of CO-emitting clouds in galaxy group environments to be strongly heated by their environments. This heating is expected to excite higher rotational J levels with high CO emissivity. Future ALMA observations of CO line fluxes at higher J levels in these galaxy groups will be critical for our understanding of the formation and evolution of such clouds.

This paper makes use of the following ALMA data: ADS/JAO.ALMA#2015.1.00860.S and ADS/JAO.ALMA#2011.0.00735.SSB. ALMA is a partnership of the ESO (representing its member states), NSF (USA), and NINS (Japan), together with the NRC (Canada), MOST and ASIAA (Taiwan), and KASI (Republic of Korea), in cooperation with the Republic of Chile. The Joint ALMA Observatory is operated by the ESO, AUI/NRAO, and NAOJ. The National Radio Astronomy Observatory is a facility of the National Science Foundation operated under cooperative agreement by Associated Universities, Inc. Massimo Gaspari is supported by NASA through Einstein Postdoctoral Fellowship Award Number PF5-160137 issued by the *Chandra* X-ray Observatory Center, which is operated by the SAO for and on behalf of NASA under contract NAS8-03060. Support for this work was also provided by *Chandra* grant GO7-18121X. HPC resources were in part provided by the NASA/Ames HEC Program (SMD-16-7320, SMD-16-7321, SMD-16-7305). Myriam Gitti thanks the Italian ARC staff in Bologna, in particular E. Liuzzo and M. Massardi, for their helpful advice during the data reduction. Myriam Gitti acknowledges partial support from PRIN-INAF 2014.

ORCID iDs

Pasquale Temi <https://orcid.org/0000-0002-8341-342X>
Massimo Gaspari <https://orcid.org/0000-0003-2754-9258>

References

- Allen, S. W., Dunn, R. J. H., Fabian, A. C., Taylor, G. B., & Reynolds, C. S. 2006, *MNRAS*, 372, 21
Amblard, A., Riguccini, L., Temi, P., et al. 2014, *ApJ*, 783, 135
Anderson, M. E., Gaspari, M., White, S. D. M., Wang, W., & Dai, X. 2015, *MNRAS*, 449, 3806

- Annibaldi, F., Bressan, A., Rampazzo, R., & Zeilinger, W. W. 2006, *A&A*, **445**, 79
- Baldi, A., Forman, W., Jones, C., et al. 2009, *ApJ*, **707**, 1034
- Barai, P., Murante, G., Borgani, S., et al. 2016, *MNRAS*, **461**, 1548
- Bertoldi, F., & McKee, C. F. 1992, *ApJ*, **395**, 140
- Bolatto, A. D., Wolfire, M., & Leroy, A. K. 2013, *ARA&A*, **51**, 207
- Braine, J., & Combes, F. 1992, *A&A*, **264**, 433
- Bregman, J. N., Miller, E. D., Athey, A. E., & Irwin, J. A. 2005, *ApJ*, **635**, 1031
- Bregman, J. N., Miller, E. D., & Irwin, J. A. 2001, *ApJL*, **553**, L125
- Brighenti, F., & Mathews, W. G. 2002, *ApJ*, **573**, 542
- Brighenti, F., Mathews, W. G., & Temi, P. 2015, *ApJ*, **802**, 118
- Caon, N., Macchetto, D., & Pastoriza, M. 2000, *ApJS*, **127**, 39
- Cappellari, M., Emsellem, E., Krajnović, D., et al. 2011, *MNRAS*, **416**, 1680
- Cavagnolo, K. W., McNamara, B. R., Nulsen, P. E. J., et al. 2010, *ApJ*, **720**, 1066
- Condon, J. J. 1997, *PASP*, **109**, 166
- Croton, D. J., Springel, V., White, S. D. M., et al. 2006, *MNRAS*, **365**, 11
- Daddi, E., Renzini, A., Pirzkal, N., et al. 2005, *ApJ*, **626**, 680
- David, L. P., Lim, J., Forman, W., et al. 2014, *ApJ*, **792**, 94
- David, L. P., Vrtilik, J., O'Sullivan, E., et al. 2017, *ApJ*, **842**, 84
- Davis, T. A., Alatalo, K., Sarzi, M., et al. 2011, *MNRAS*, **417**, 882
- Diniz, S. I. F., Pastoriza, M. G., Hernandez-Jimenez, J. A., et al. 2017, *MNRAS*, **470**, 1703
- Edge, A. C. 2001, *MNRAS*, **328**, 762
- Emsellem, E., Cappellari, M., Krajnović, D., et al. 2011, *MNRAS*, **414**, 888
- Fabian, A. C. 2012, *ARA&A*, **50**, 455
- Feldmann, R., Carollo, C. M., Mayer, L., et al. 2010, *ApJ*, **709**, 218
- Filho, M. E., Fraternali, F., Markoff, S., et al. 2004, *A&A*, **418**, 429
- Gaspari, M., Brighenti, F., & Temi, P. 2012, *MNRAS*, **424**, 190
- Gaspari, M., Brighenti, F., & Temi, P. 2015, *A&A*, **579**, A62
- Gaspari, M., McDonald, M., Hamer, S. L., et al. 2017a, arXiv:1709.06564
- Gaspari, M., Melioli, C., Brighenti, F., & D'Ercole, A. 2011, *MNRAS*, **411**, 349
- Gaspari, M., Ruszkowski, M., & Oh, S. P. 2013, *MNRAS*, **432**, 3401
- Gaspari, M., & Sądowski, A. 2017, *ApJ*, **837**, 149
- Gaspari, M., Temi, P., & Brighenti, F. 2017b, *MNRAS*, **466**, 677
- Giacintucci, S., O'Sullivan, E., Vrtilik, J., et al. 2011, *ApJ*, **732**, 95
- Gitti, M., Brighenti, F., & McNamara, B. R. 2012, *AdAst*, **2012**, 950641
- Goulding, A. D., Greene, J. E., Ma, C.-P., et al. 2016, *ApJ*, **826**, 167
- Gozaliasl, G., Finoguenov, A., Khosroshahi, H. G., et al. 2016, *MNRAS*, **458**, 2762
- Haardt, F., & Madau, P. 2012, *ApJ*, **746**, 125
- Hirashita, H., & Nozawa, T. 2017, arXiv:1701.07200
- Hogan, M. T., McNamara, B. R., Pulido, F., et al. 2017, *ApJ*, **837**, 51
- Jones, C., Forman, W., Vikhlinin, A., et al. 2002, *ApJL*, **567**, L115
- Lau, E. T., Gaspari, M., Nagai, D., & Coppi, P. 2017, arXiv:1705.06280
- Li, Y., & Bryan, G. L. 2014, *ApJ*, **789**, 54
- Li, Y., Bryan, G. L., Ruszkowski, M., et al. 2015, *ApJ*, **811**, 73
- Lim, J., Dinh-V-Trung, Vrtilik, J., David, L. P., & Forman, W. 2017, arXiv:1710.06186
- Machacek, M. E., Jerius, D., Kraft, R., et al. 2011, *ApJ*, **743**, 15
- Mahdavi, A., Trentham, N., & Tully, R. B. 2005, *AJ*, **130**, 1502
- Mathews, W. G., & Brighenti, F. 2003, *ApJL*, **590**, L5
- Mathews, W. G., Temi, P., Brighenti, F., & Amblard, A. 2013, *ApJ*, **768**, 28
- McCourt, M., Sharma, P., Quataert, E., & Parrish, I. J. 2012, *MNRAS*, **419**, 3319
- McDonald, M., Veilleux, S., & Mushotzky, R. 2011, *ApJ*, **731**, 33
- McMullin, J. P., Waters, B., Schiebel, D., Young, W., & Golap, K. 2007, in ASP Conf. Ser. 376, *Astronomical Data Analysis Software and Systems XVI*, ed. R. A. Shaw, F. Hill, & D. J. Bell (San Francisco, CA: ASP), **127**
- McNamara, B. R., & Nulsen, P. E. J. 2007, *ARA&A*, **45**, 117
- McNamara, B. R., & Nulsen, P. E. J. 2012, *NJPh*, **14**, 055023
- McNamara, B. R., Russell, H. R., Nulsen, P. E. J., et al. 2016, *ApJ*, **830**, 79
- Mei, S., Blakeslee, J. P., Côté, P., et al. 2007, *ApJ*, **655**, 144
- Merritt, D., & Ferrarese, L. 2001, *MNRAS*, **320**, L30
- Molendi, S., Tozzi, P., Gaspari, M., et al. 2016, *A&A*, **595**, A123
- Nagar, N. M., Falcke, H., & Wilson, A. S. 2005, *A&A*, **435**, 521
- Ogorzalek, A., Zhuravleva, I., Allen, S. W., et al. 2017, arXiv:1702.04364
- O'Sullivan, E., Combes, F., Hamer, S., et al. 2015, *A&A*, **573**, A111
- O'Sullivan, E., Ponman, T. J., Kolokythas, K., et al. 2017, *MNRAS*, **472**, 1482
- Peterson, J. R., & Fabian, A. C. 2006, *PhR*, **427**, 1
- Peterson, J. R., Kahn, S. M., Paerels, F. B. S., et al. 2003, *ApJ*, **590**, 207
- Pulido, F. A., McNamara, B. R., Edge, A. C., et al. 2017, arXiv:1710.04664
- Rampazzo, R., Panuzzo, P., Vega, O., et al. 2013, *MNRAS*, **432**, 374
- Revaz, Y., Combes, F., & Salomé, P. 2008, *A&A*, **477**, L33
- Salomé, P., & Combes, F. 2003, *A&A*, **412**, 657
- Sarzi, M., Alatalo, K., Blitz, L., et al. 2013, *MNRAS*, **432**, 1845
- Sharma, P., McCourt, M., Quataert, E., & Parrish, I. J. 2012, *MNRAS*, **420**, 3174
- Smith, D. J. B., Dunne, L., da Cunha, E., et al. 2012, *MNRAS*, **427**, 703
- Sun, M. 2012, *NJPh*, **14**, 045004
- Temi, P., Brighenti, F., & Mathews, W. G. 2007a, *ApJ*, **660**, 1215
- Temi, P., Brighenti, F., & Mathews, W. G. 2007b, *ApJ*, **666**, 222
- Temi, P., Brighenti, F., & Mathews, W. G. 2009, *ApJ*, **695**, 1
- Tonry, J. L., Dressler, A., Blakeslee, J. P., et al. 2001, *ApJ*, **546**, 681
- Trager, S. C., Faber, S. M., Worthey, G., & González, J. J. 2000, *AJ*, **120**, 165
- Trinchieri, G., & Goudfrooij, P. 2002, *A&A*, **386**, 472
- Valentini, M., & Brighenti, F. 2015, *MNRAS*, **448**, 1979
- van der Wel, A., Franx, M., van Dokkum, P. G., et al. 2005, *ApJ*, **631**, 145
- Vantyghem, A. N., McNamara, B. R., Edge, A. C., et al. 2017, *ApJ*, **848**, 101
- Voit, G. M., Donahue, M., Bryan, G. L., & McDonald, M. 2015, *Natur*, **519**, 203
- Voit, G. M., Meece, G., Li, Y., et al. 2017, *ApJ*, **845**, 80
- Vollmer, B., Thierbach, M., & Wielebinski, R. 2004, *A&A*, **418**, 1
- Werner, N., Oonk, J. B. R., Sun, M., et al. 2014, *MNRAS*, **439**, 2291
- Ziegler, B. L., Thomas, D., Böhm, A., et al. 2005, *A&A*, **433**, 519